Master Thesis

Quantitative evaluation of muon track matching efficiency with Muon Forward Tracker and Muon Spectrometer at LHC-ALICE

Kaede Kamano

18810015

High Energy Physics Laboratory,
Department of Mathmatical and Physical Sciences,
Graduate School of Humanities and Science,
Nara Women's University

March 27, 2020

Abstract

ALICE has been researching physics in extremely high temperature and high dense matter that is generated by heavy-ion collision using LHC. One of them is to understand the mass generation mechanism by the chiral symmetry breaking. The measurement target is low mass vector mesons that decay dimuon. Extensive efforts in the ALICE upgrade projects are currently being made toward LHC-Run3 (2021-2024). One of the new detectors is the Muon Forward Tracker (MFT) that consists of 5 disks made of silicon pixel detectors that have high position resolution. MFT is newly installed in the Muon Spectrometer (MUON). MUON has the hadron absorber in front of the detector so that there is no way to get the track information before the absorber. Muon has been measured the way to extrapolate the muon track measured by MUON to the vertex. In this method, there are problems with the track angles measurements that affect the invariant mass measurements especially in low p_T regions that is greatly affected by the multiple scattering effects in the absorber. Track performance and rejection power of muon from hadron decay are improved by installing MFT between the vertex and the absorber.

Track matching between MFT and MUON is crucial to improve the invariant mass resolution and reject muons from hadron decays in the hadron absorber. Track matching is connecting the same muon track before and after the absorber with MFT and MUON. In the experiment, the MUON track is extrapolated through the absorber towards the primary vertex, and the best MFT track is chosen to connect with that MUON track at the last MFT plane. In this study, the track matching algorithm between MFT and MUON is developed and evaluated. We need to consider the multiple scattering effects in the absorber in the track matching. Multiple scattering effects of muons in the absorber is simulated, and the correlation distribution of track position and angle of the muons measured by MUON at the collision point side of the absorber, that is, on the MFT side. The size of the search window depends on the momentum of the muon track and the center of the distribution of the track position and angle depends on the position and angle of the muon track measured by MUON. To use the same track matching algorithm in various momentum regions, the correlation distribution of the position and angle is normalized and the matching parameter R that can be used regardless of momentum is developed. As a result, the background is significantly reduced.

Contents

List of Figures

List of Tables

1 Introduction

1.1 Standard model

There are four fundamental forces which are gravitational, electromagnetic, strong and weak interactions. The standard model is the theory that describes the three of the four fundamental forces, electromagnetic, strong, and weak interactions. All matter in the world is made of atoms. Atom is made of nucleus and electrons. Nucleus is made of protons and neutrons. Proton and neutron are made of quarks which are one of the elementary particles. Elementary particle is the smallest component of matter. Elementary particles of the standard model consist of elementary fermions and elementary bosons. Fermions are classified into (anti-)quarks and (anti-)leptons, which follow the Pauli exclusion principle. Bosons are classified into gauge bosons and scalar bosons. Gauge bosons are force carriers that mediate the strong, weak, and electromagnetic interactions. Scalar bosons, namely higgs bosons, give other particles their mass. Figure 1 shows the elementary particles of the standard model.

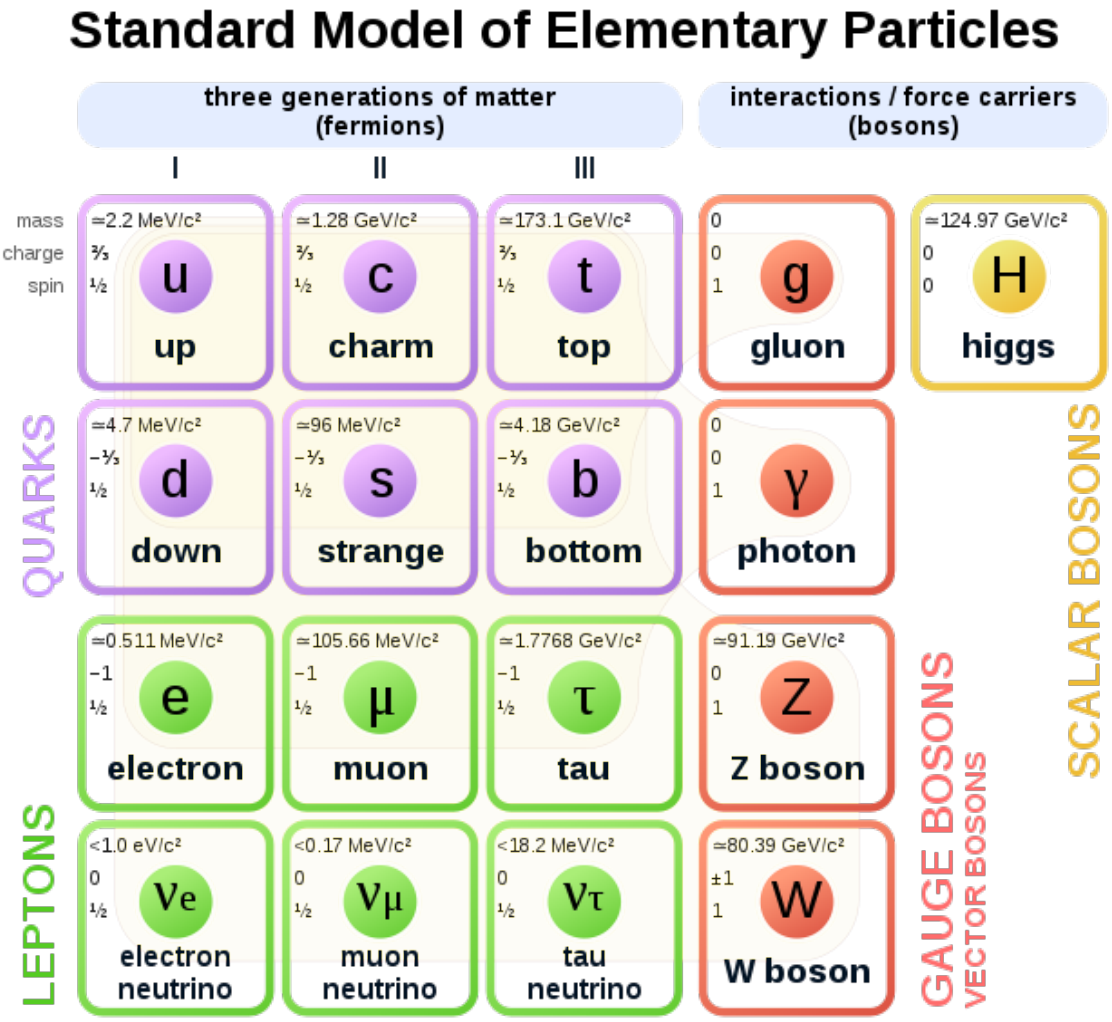

Figure 1: Elementary particles of the standard model.

1.2 Quantum Chromodynamics

The quantum chromodynamics (QCD) is the theory that describes the strong interaction between quarks and gluons. QCD has two main properties such as color confinement and asymptotic freedom. Quarks and gluons have a color charge. Color charge is described by analogy to the primary colors of light (red, green and blue). When a particle does not have a color charge, it is called "white". The strong interaction is mediated by exchanging gluons that carry color charges. The strong force increases when the distance between color charges is larger. The distance between color charges is beyond some critical distance, a new quark and anti-quark pair pop up from the vacuum. Therefore, quark can not exist by itself, and observed hadrons are always "white". This property is called color confinement. While the strong interaction decreases when the distance between color charges is smaller, and quarks and gluons can move freely like free particles. Quarks and gluons are not confined in hadrons under extremely high temperature and/or density. This property is called asymptotic freedom.

1.3 Quark-Gluon Plasma

Quark-gluon plasma (QGP) is a state of matter where quarks and gluons are no longer confined in hadrons under extremely high temperature and/or density. QGP is believed to exist in the primordial universe up to a few microseconds after Big Bang or in neutron stars, as shown in Figure 2. Lattice QCD predicts the critical temperature T_c between hadronic state and QGP state is $T_c \sim 160$ MeV. QGP can be created experimentally by momentarily generating high temperature and high pressure by high energy heavy ion collision.

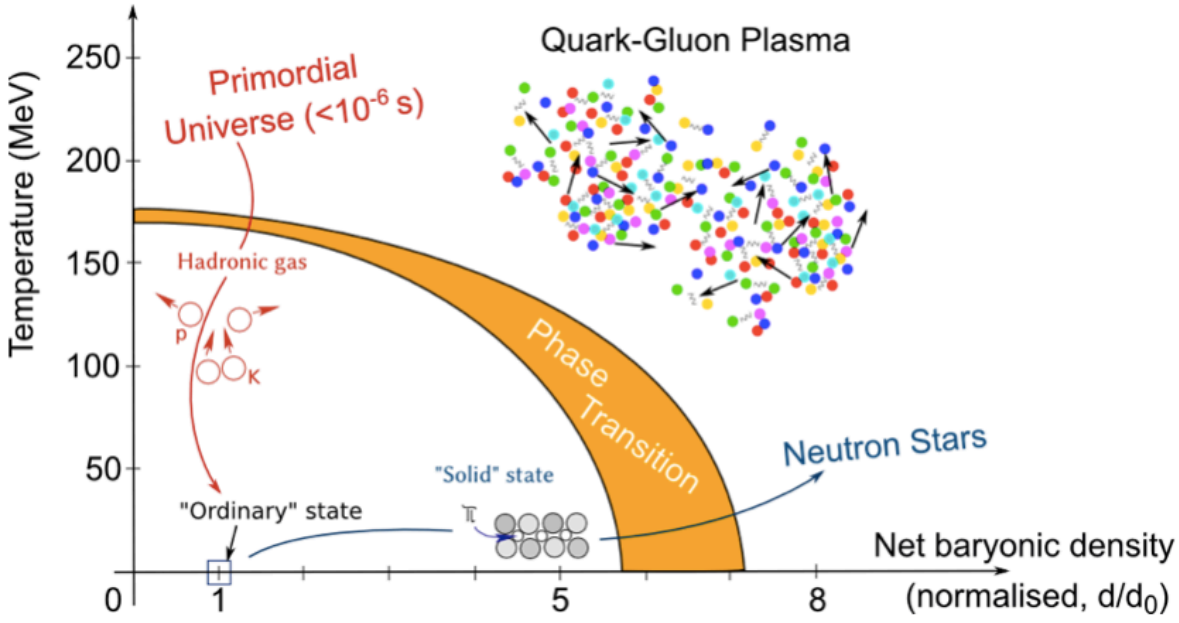

Figure 2: Phase diagram of QCD matter. [4]

1.4 High energy heavy-ion collisions

To create QGP, particle accelerators deliver relativistic high energy head-on collisions between massive ions such as gold or lead nuclei. The collisions are dynamical processes with a very short time scale. Figure 3 shows the time evolution of a high energy heavy ion collision. The temperature scale of high energy heavy ion collision is 100 MeV $\sim 10^{12}$ K, and the timescale is 10 fm/c $\sim 10^{-23}$ seconds.

Initial state

Nuclei are accelerated at close to the speed of light. Therefore the thickness of nuclei shrinks to $1/\gamma$ in direction of travel due to Lorentz contraction.

Pre-QGP

Partons that are constituents of nuclei interact by collision. A reaction surface that is a high density is made where the partons collide. Quarks and gluons are excited by this energy and scattered.

QGP state

Due to the repeated scattering of quarks and gluons on the reaction surface, the system reaches thermalization and the temperature of the system rises above the phase transition temperature T_c. Above T_c, quarks and gluons are not confined in hadrons, which is called QGP state.

Hadronization

Over time, the system begins to cool, and hadrons are generated from partons. In this state, the ratio of particles is not fixed yet because inelastic collisions between particles still exist. The temperature at which particle ratio is fixed is called the chemical freeze-out temperature T_{ch}. The system continues to expand, at some point, particles stop interacting with each other, which is called kinematic freeze-out. The temperature of this state is called the kinematic freeze-out temperature T_{fo}. Hadrons travel and will be observed by detectors.

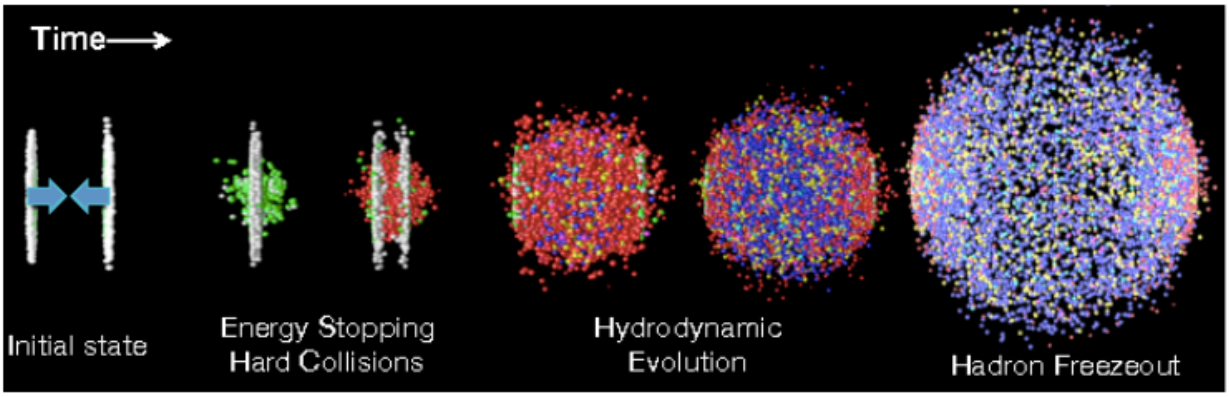

Figure 3: The time evolution of a high energy heavy ion collision. [5]

1.5 Chiral symmetry breaking and its restoration

To understand chiral symmetry breaking and its restoration in QGP is one of the important research tasks in physics. Proton and neutron are made of quarks. The mass of the proton is $m_p \sim 988$ MeV/c^2. The valence quarks of the proton are two up quarks ($m_u \sim 2.4$ MeV/c^2) and one down quark ($m_d \sim 4.8$ MeV/c^2). The total mass of the valence quarks is just 2% of the proton mass. The quark mass arises out of the Higgs mechanism.[6] The rest of the proton mass arises out of chiral symmetry breaking. As the universe cooled after Big Bang, pair of quark and anti-quark was condensed in the vacuum by Bose-Einstein condensation. Therefore vacuum is no longer empty but filled with a medium that has quark condensate. When matter moves, the matter has to thrust quark condensate. This is the mechanism to give matter its mass. This transition from an empty vacuum to a vacuum filled with the quark condensate is called the chiral symmetry breaking.

To probe the mass generation mechanism by the chiral symmetry breaking, what should we observe? The quark condensate itself is not observable, but its strength depends on temperature and density. Figure 4 shows the strength of the quark condensate depending on temperature and density. We have two methods to prove the mass generation mechanism by the chiral symmetry breaking. First is to create an extremely high-temperature matter (such as QGP) by colliding nuclei accelerated at close to the speed of light, and examine a mass distribution of matter inside the extremely high-temperature matter. Second is to inject particles whose character is well known into a nucleus, which is supposed to be a high-density medium, and examine the mass difference between the particles before and after. [7]

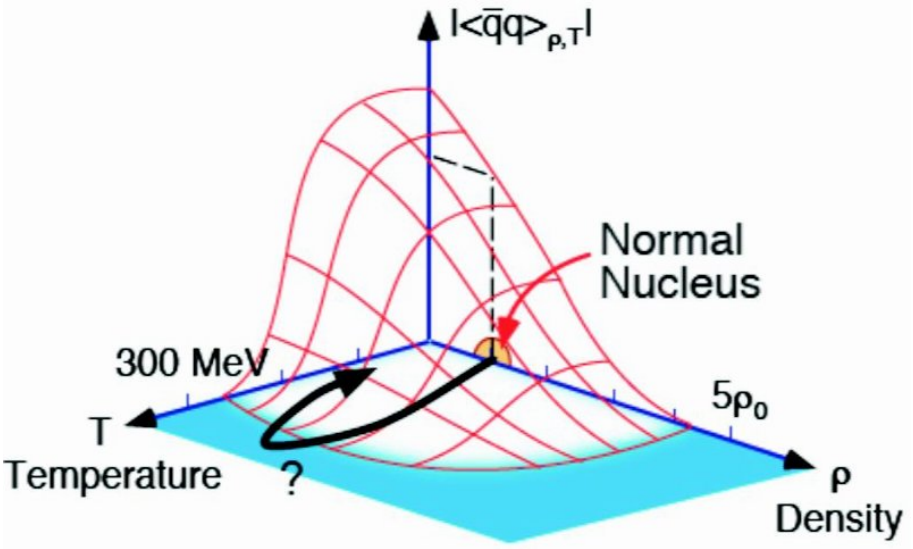

Figure 4: Quark mass in the QCD vacuum and the Higgs vacuum. Horizontal axis shows total quark mass and vertical axis shows mass that arise out of the Higgs mechanism. [8]

1.6 Low mass vector meson

Low mass vector mesons ω and ϕ are some of the good tools to observe the mass modifications due to the chiral symmetry restoration. ω and ϕ mesons have a short lifetime, therefore they are likely to decay in QGP that is the extremely high-temperature matter where the strength of the quark condensate is smaller. ω and ϕ mesons have dimuon decay mode. Dimuon is not affected by the strong interaction in QGP. Low mass vector mesons ω and ϕ mesons consist of light quarks. Figure 5 shows masses that arise out of the Higgs mechanism vs total quark mass. Total quark mass is the quark mass in the QGP vacuum. Masses of heavy quarks (c, t, b) are almost exclusively generated through their coupling to the Higgs field, while masses of light quarks (u, d, s) are dominated by the spontaneous chiral symmetry breaking. Therefore ω and ϕ are suited to observe the mass modifications due to the chiral symmetry restoration.

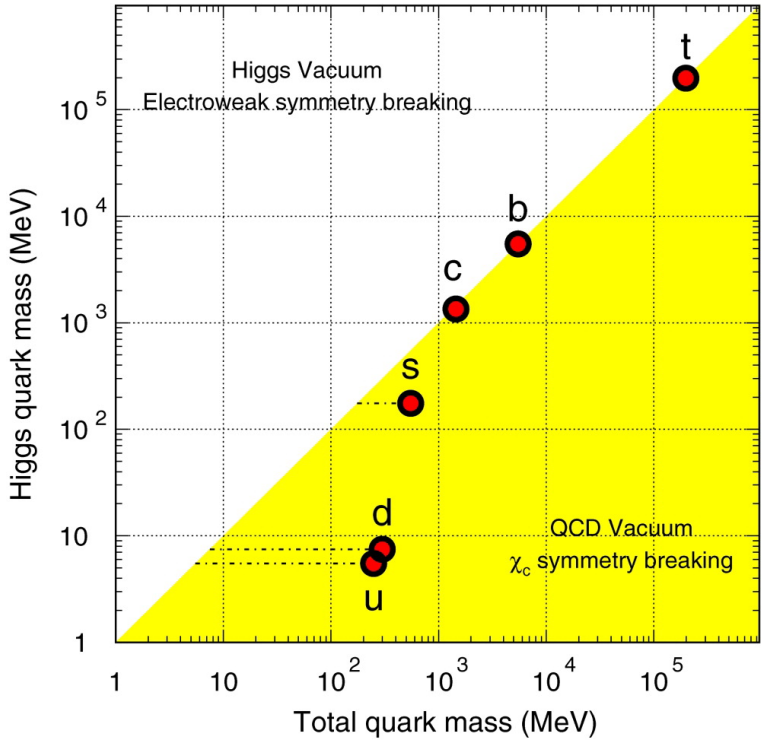

Figure 5: Quark mass in the QCD vacuum and the Higgs vacuum. Horizontal axis shows total quark mass and vertical axis shows mass that arise out of the Higgs mechanism. [9]

1.7 Previous research

In-medium modification of the ϕ meson at normal nuclear density has been measured by KEK-PS E235 collaboration (2007). KEK-PS E325 was conducted at the KEK 12 GeV Proton-Synchrotron. Proton beam was injected to the fixed copper and carbon targets to search for in-medium mass modifications of vector meson in the reaction 12 GeV $p + A \rightarrow \phi + X \rightarrow e^+e^- + X'$. Figure 6 shows the e^+e^- distribution from ϕ meson. A significant excess on the low-mass side of the ϕ meson peak in observed in the low $\beta\gamma(= \beta/\sqrt{1-\beta^2})$ region of ϕ meson ($\beta\gamma < 1.25$) with copper targets (Figure 6 upper right). This observation is consistent with the picture of the ϕ modification in the nucleus. Thus, this study is one of the results that experimentally verified vector meson mass modification at normal nuclear density.

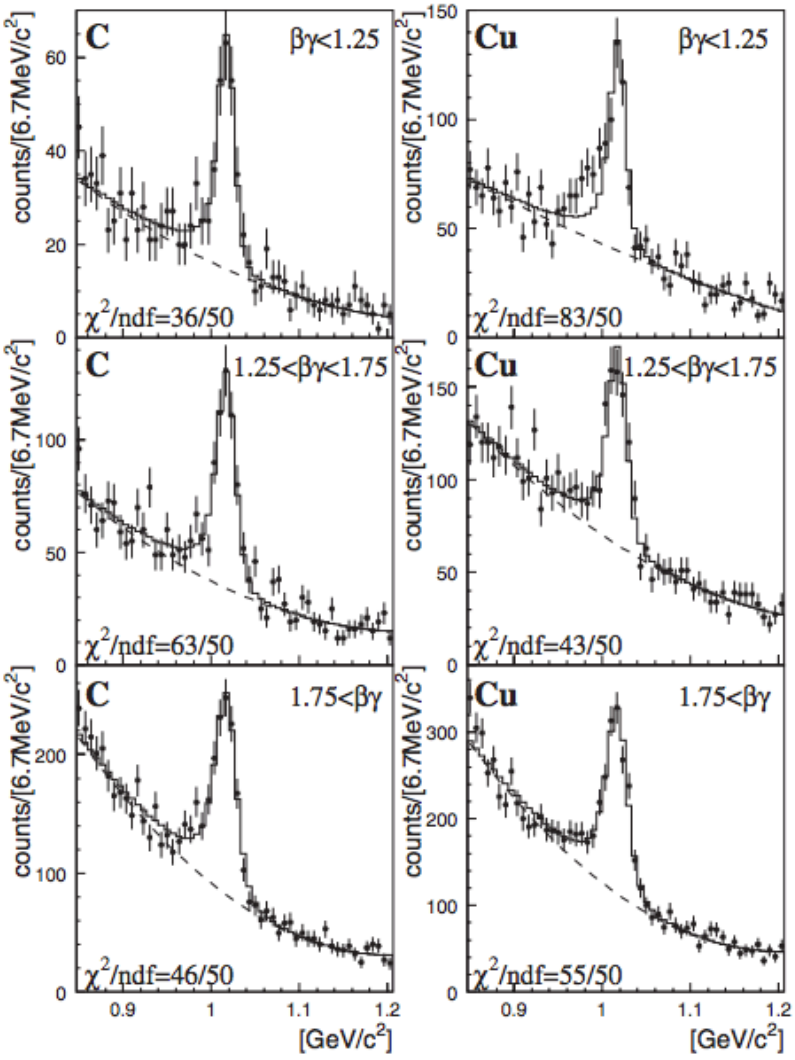

Figure 6: Obtained e^+e^- distribution with fit result by KEK-PS E325 collaboration. The points with error bars represent the data. The solid lines represent the fit results with an expected $\phi \to e^+e^-$ shape and quadratic background. The dashed lines represents the background. [10]

1.8 Motivation

Partial restoration of chiral symmetry is expected to occur in an extremely high-temperature matter such as QGP or a high-density medium such as a nucleus. Chiral symmetry restoration in QGP has not been observed yet. Low mass vector mesons ω and ϕ that have dimuon decay mode are one of the good tools to observe the mass modifications due to the chiral symmetry restoration in QGP. High mass resolution is needed to observe the mass modification. The Muon Forward Tracker, a new silicon tracking detector installed in the existing muon detector in ALICE, will deliver a better mass resolution. Mass resolution is determined by tracking accuracy between new and old detectors. In this study, the development and evaluation of the track matching between new and old detectors using the correlation between track position and angle are discussed.

2 Experimental setup

2.1 Large Hadron Collider

At the Large Hadron Collider (LHC), the beam will stop for months to years between physics experiments. This period is for maintenance and upgrades for the accelerators and detectors. The LHC is the most powerful particle collider built at the European Organization for Nuclear Research (CERN) in 2008. The LHC consists of a 27-kilometer ring of superconducting magnets with several accelerating structures to boost the energy of the particles. Two high energy hadron beams are accelerated at close to the speed of light before they are made to collide. There are four main detectors located underground at the LHC's interaction points that are ATLAS, CMS, LHCb, and ALICE.

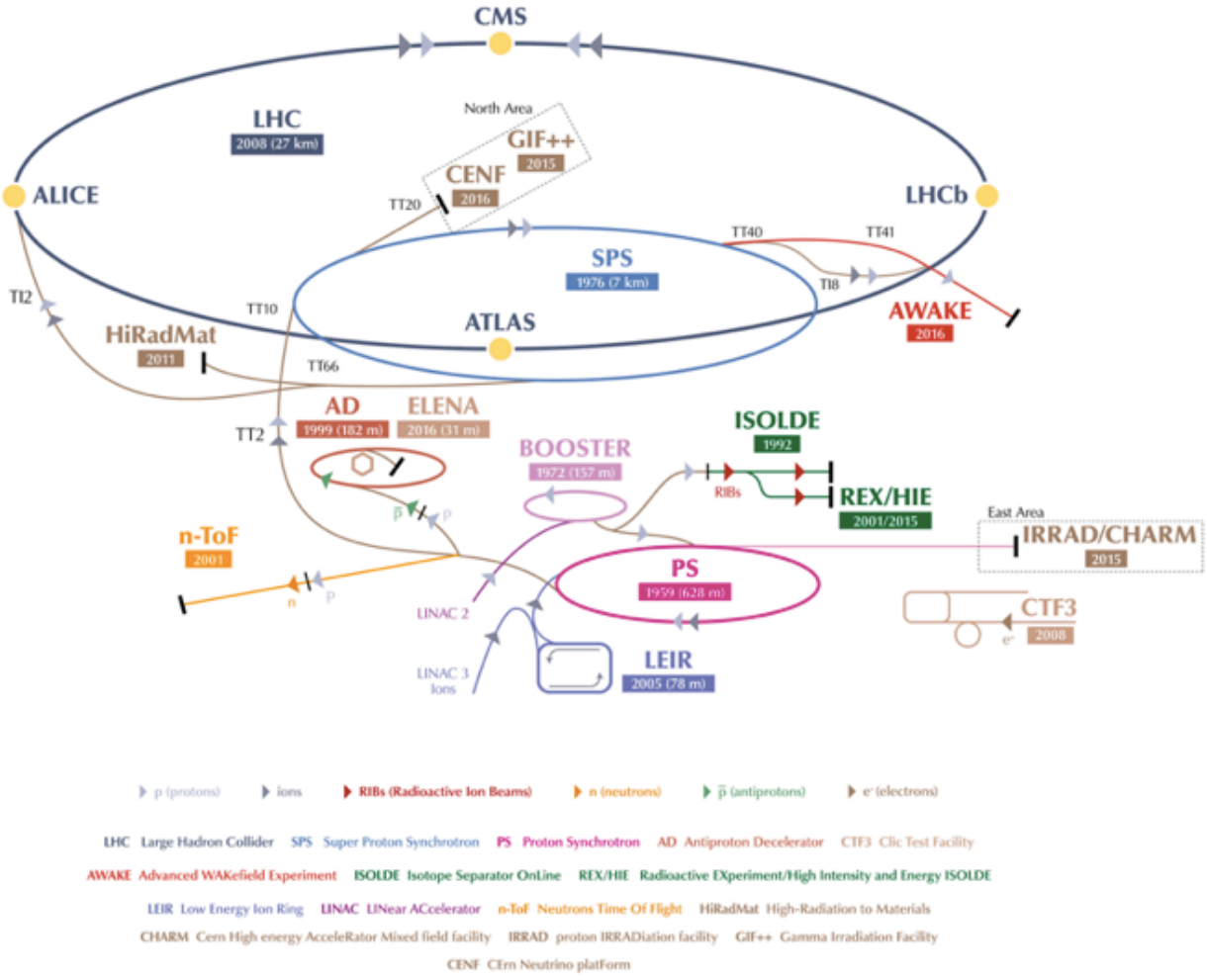

Figure 7: The CERN accelerator complex. [11]

2.1.1 LHC schedule

The LHC is shut down for two years from 2019 to the end of 2020 (Long Shutdown 2, LS2) as shown in Figure 8. The ALICE collaboration is currently working for a major upgrade during LS2. The new ALICE will have enhanced read-out capabilities and improved accuracy and efficiency in tracking particles and identifying the interaction vertex. The Muon Forward Tracker is also installed during LS2. The LHC will restart in 2021 and run until the end of 2024 (Run 3).

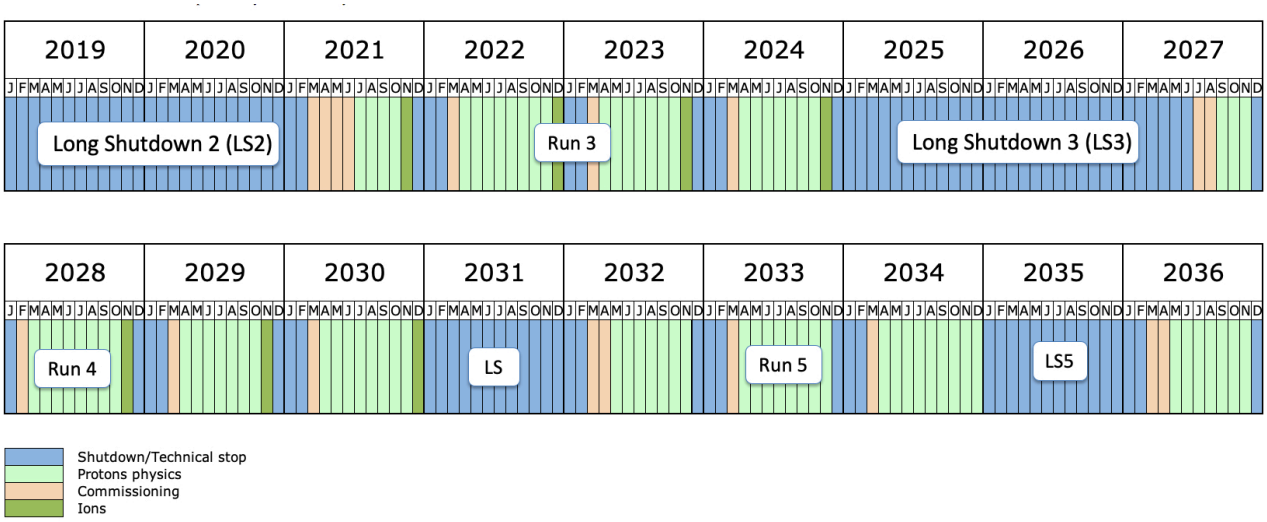

Figure 8: Long term LHC schedule. [12]

2.2 ALICE Detector

ALICE (A Large Ion Collider Experiment) has been designed to study QGP in heavy ion collisions at LHC. High energy heavy ion collision experiment is the only experiment to access extremely high temperature and density where QGP is created. About twenty detectors are set to detect various particles created by the heavy ion collisions. Extensive efforts in the ALICE upgrade projects are currently being made toward LHC-Run3 (2021-2024). Figure 9 shows the 3D schematic of ALICE detector for LHC-Run3. The height of the ALICE detector is approximately 16 m and length is 20 m. Beam axis is defined as z axis, and the other horizontal axes are defined as x and y axes. The center of the ALICE detector is defined (x,y,z)=(0,0,0).

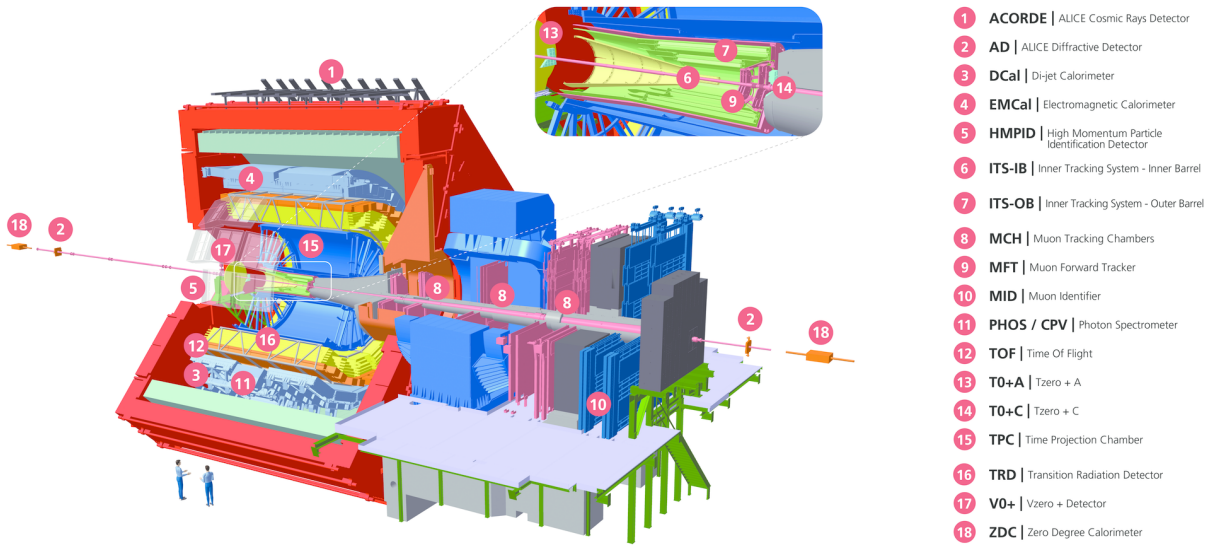

Figure 9: 3D schematic of ALICE detector for LHC-Run3.

2.2.1 Muon Spectrometer (MUON)

Identification and measurement of muons in ALICE are currently performed by the Muon Spectrometer (MUON) shown as 8 and 10 in Figure 9. MUON consists of a hadron absorber (shown as Front absorber in Figure 10), a dipole magnet, five tracking chambers, an iron wall and two trigger chambers. The schematic illustration of MUON is shown in Figure 10. MUON acceptance covers the pseudo-rapidity region $-4.0 < \eta < -2.5$. The hadron absorber made of carbon, concrete and steel suppresses all particles except muons coming from vertex. It is placed between z = -0.9 m and z = -5.03 m, and the material budget corresponds to $\sim 60X_0$ ($\sim 10\lambda_{int}$). The hadron absorber provides a reliable muon filter for momenta above 4 GeV/c ($p_T \sim 0.5$ GeV/c). Table 1 summaries the geometrical parameter of the hadron absorber. A dipole magnet provides a magnetic field of 0.7 T in horizontal direction. A 1.2 m ($\sim 7.2\lambda_{int}$) thick iron wall is placed between tracking (TRK1-5) and trigger (TRG1-2) systems as shown in Figure 10. The iron wall absorbs the residual secondary hadrons emerging from the hadron absorber.

Table 1: Geometrical parameters of the hadron absorber.

Material	Length (cm)	Radiation length (cm)
Carbon	225	18.8
Concrete	126	10.7
Steel	62	1.76
Total	413	-

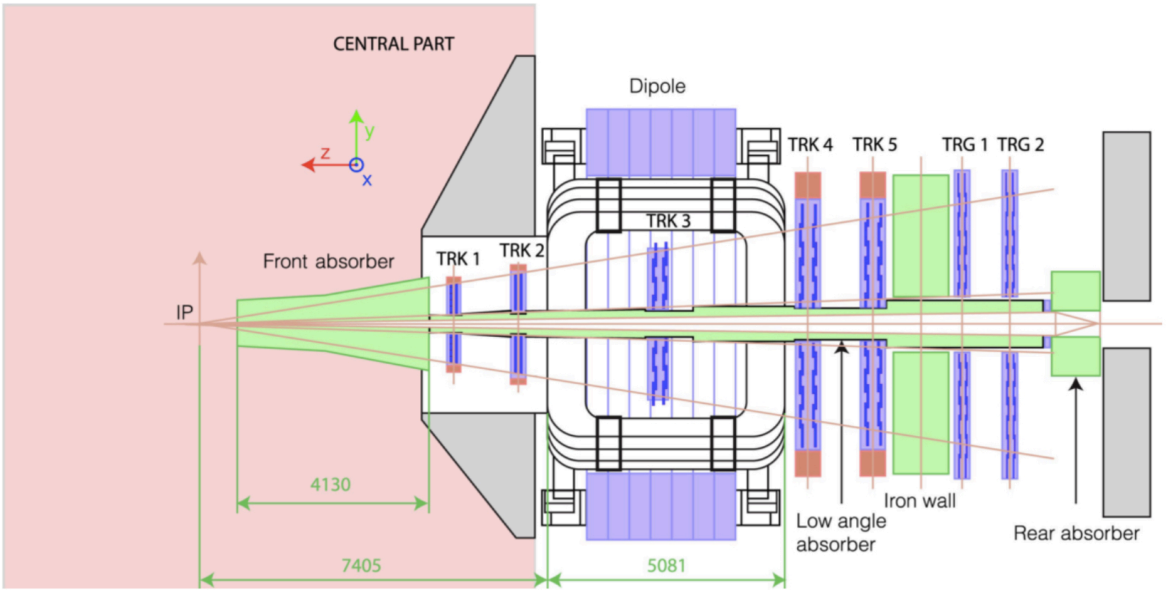

Figure 10: Schematic illustration of the ALICE Muon Spectrometer.[2]

MUON has provided a wealth of results. However, MUON has an critical limitation that track information around the vertex region is not available. This is due to the large distance of the tracking stations from the primary vertex and the multiple scattering in the hadron absorber. The detail tracking information around the vertex region are completely smeared out, therefore we have very limited possibilities to reject muons coming from semi-muonic decays of pions and kaons that is an major background both in single muon and dimuon analyses especially at low masses and/or low p_T. Also, the lack of details in the vertex region prevents us to disentangle prompt and displaced J/ψ production. Besides, the degradation of the track direction resolution due to multiple scattering in the hadron absorber greatly affects the mass resolution especially at low masses in the region of ω and ϕ mesons.

2.2.2 Muon Forward Tracker (MFT)

The Muon Forward Tracker (MFT) is a silicon pixel director added between the primary vertex and the hadron absorber of the Muon Spectrometer, shown as 9 in Figure 9. MFT acceptance covers the pseudo-rapidity region $-3.6 < \eta < -2.45$. Figure 11 shows the schematic illustration of a muon tracker in ALICE until LHC-Run 2 (top) and from LHC-Run 3 (bottom). MFT gives access to new measurements that are not possible with the LHC-Run 2 MUON setup. The basic idea of MFT is to match the extrapolated muon tracks coming from the tracking chambers (MUON) after the hadron absorber with the tracks measured in MFT planes before the hadron absorber. Track around the primary vertex is available by track matching between MFT and MUON. That gives us a better mass resolution and rejection of muons from decay hadrons.

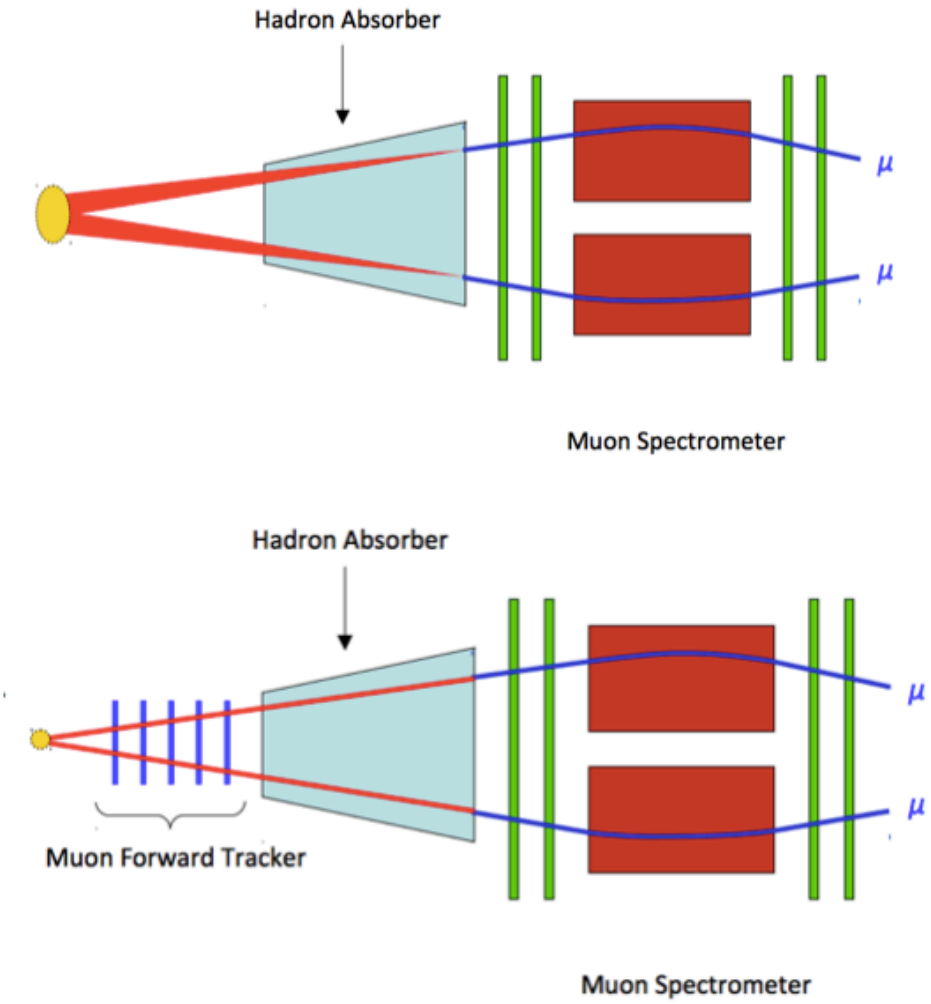

Figure 11: Schematic illustration of muon tracker in ALICE (top) until LHC-Run 2 and (bottom) from LHC-Run 3. [13]

MFT consists of two half-MFT cones. Figure 12 shows the general layout of MFT half-cone. Each half-MFT cone consists of 5 half-disks positioned along the beam axis. A half-disk consists of a disk spacer, a disk support, two printed circuit boards and the sensor ladders. Table 2 summarizes the geometrical parameters of MFT. The sensor ladders consists of silicon pixel sensors soldered to a Flex Printed Circuit with aluminum strips. Figure 13 shows the half-disk-0. Table 3 summarizes the main specification of MFT sensors.

Physics program with MFT

Some physics that can be measured with MFT are described below.

- Evaluation of the medium temperature and study of charmonium dissociation and regeneration mechanism via measurements of prompt J/ψ and $\psi^{'}$ production and

elliptic flow.

- Study of the degree of thermalization of heavy quarks in the medium via measurements of heavy flavor and charmonium elliptic flow.
- Extract of the energy density of the medium, the color charge and mass dependence of parton in medium energy loss via measurements of heavy quark production separately for charm and beauty in the single muon channel and J/ψ from b-hadron decay.
- Investigation of the chiral nature of the phase transition via measurement of low mass vector mesons.

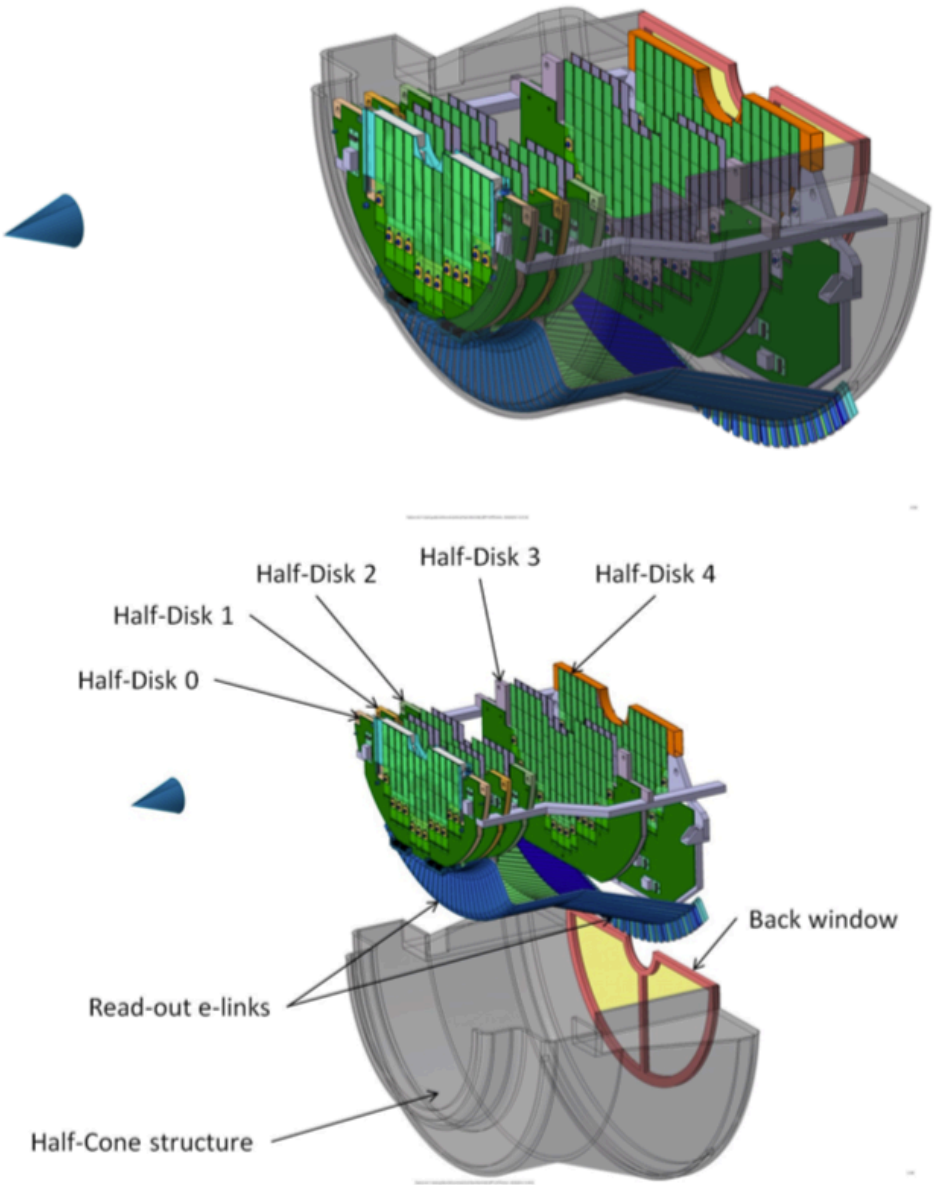

Figure 12: General layout of MFT Half-Cone. [1]

Table 2: Geometrical parameters of MFT. [1]

Half-Disk	0	1	2	3	4	Full MFT
Inner radius (mm)	25.0	25.0	25.0	38.2	39.2	-
Outer radius (mm)	92.6	98.0	104.3	130.1	143.5	-
z-position (mm)	-460	-493	-531	-687	-768	-
No. sensors	64	64	76	112	132	896

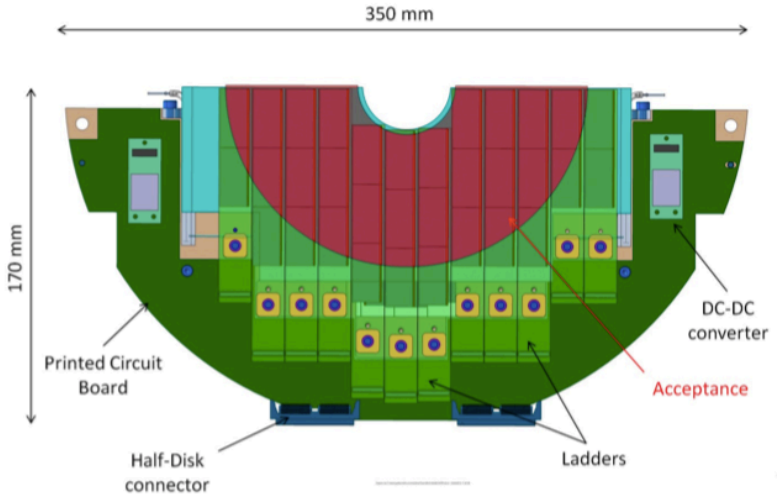

Figure 13: Half-disk-0. [1]

Table 3: Main specification for MFT sensors [1]

Parameter	Value
Spatial resolution	$\sim 5\mu m$
Pixel pitch	$\sim 25\mu m$
Detection efficiency	$> 99.5\%$
Integration time	$< 20\mu m$
Sensor thickness	$50\mu m$
Binary output	1-bit
Power dissipation	< 150 mW/cm^2

3 Development of MFT-MUON track matching

3.1 Tracking with MFT and MUON

Figure 14 (left) shows the tracking flow with the MFT and MUON. Tracks are reconstructed by MFT and MUON separately. Most MFT tracks are from hadrons. Hadrons stop at the absorber and only muons can go through the absorber. MFT that placed upstream of the absorber has hundreds of tracks, while MUON that placed downstream of the absorber has only several tracks. To reconstruct Global MFT/MUON tracks, the best MFT track should be selected from MFT track candidates for one MUON track. The MUON track is extrapolated throughout the absorber towards the primary vertex. The search window is then determined at the last MFT plane taking into account the effect of multiple scattering and energy loss in the hadron absorber as shown in Figure 14 (right). When the momentum of the MUON track is smaller, the search window becomes larger due to the effect of multiple scattering and the number of the MFT track candidates becomes larger. The MFT tracks in the search window are the matching candidates one of which is supposed to match a MUON track. A matching quality parameter of each MFT track candidate is calculated for a MUON track. A matching quality parameter is explained in Section 4. The MFT track candidate that has the best matching quality is selected as the best MFT track.

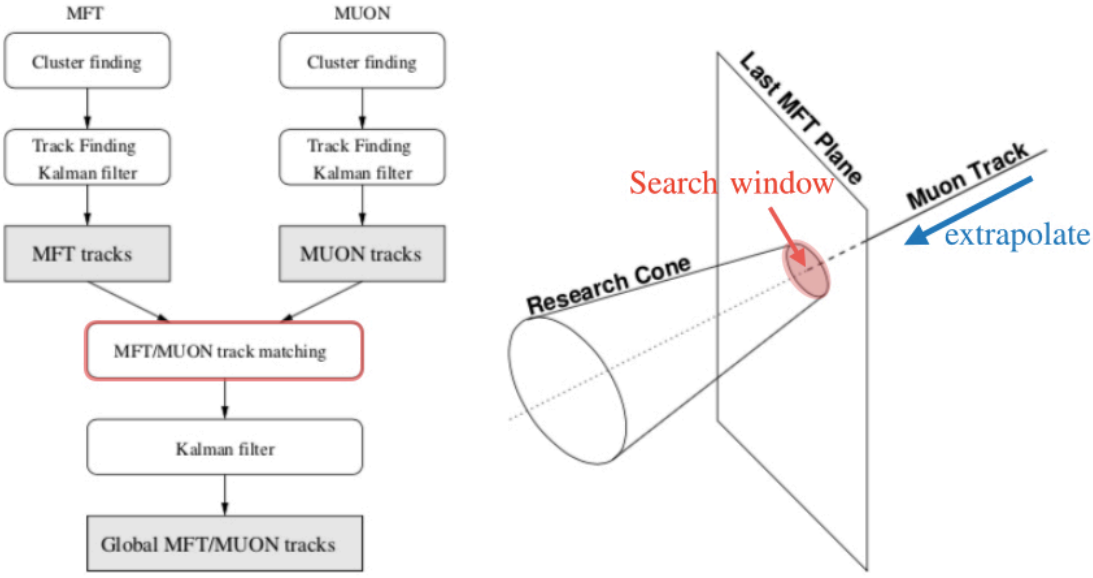

Figure 14: Schematic illustration of the MFT / MUON reconstruction stages (left) and schematic illustration of the MFT / MUON matching search window (right). [1]

3.2 Number of MFT track candidates for MUON track

The number of the MFT track candidates at the last MFT plane with the MUON track extrapolated throughout the hadron absorber is calculated as below. The number of candidates $< N >$ at arbitrary pseudo-rapidity is calculated as:

$$< N >= \sigma(r) * h_x * h_y \tag{1}$$

where $\sigma(r)$ is the number of injected per unit area at the arbitrary pseudo-rapidity particles calculated from multiplicity. h_x and h_y are the width of the search windows of x and y directions respectively that is calculated from multiple scattering.

3.2.1 Multiplicity

In this calculation, charged-particle pseudo-rapidity density in 0-5% centrality classes in Pb-Pb collision at $\sqrt{s_{NN}} = 5.02$ TeV measured by ALICE shown in Figure 15 is used.

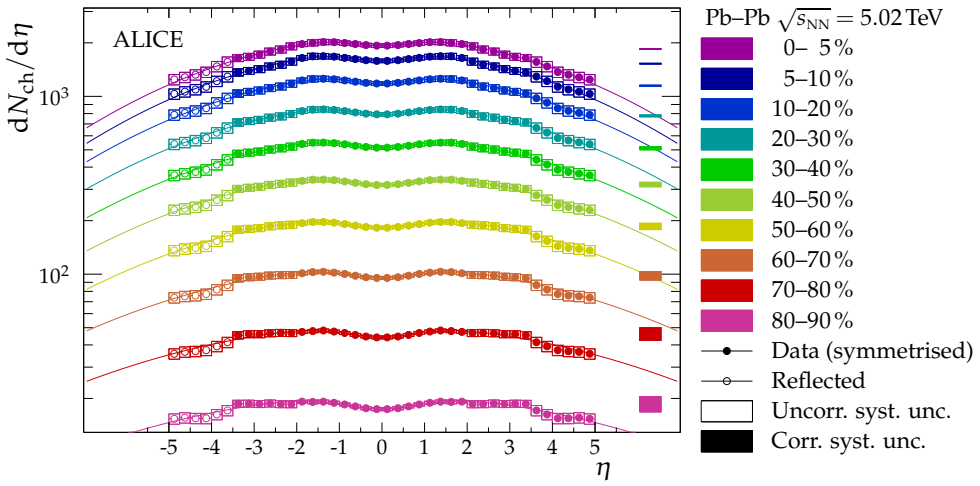

Figure 15: Charged-particle pseudo-rapidity density for ten centrality classes over a broad η range in Pb-Pb collisions at $\sqrt{s_{NN}} = 5.02$ TeV. Boxes around the points reflect the total uncorrelated systematic uncertainties, while the filled squares on the right reflect the correlated systematic uncertainty (evaluated at η=0). Statistical errors are generally insignificant and smaller than the markers. [14]

To obtain the number of injected particles per unit area at the last MFT plane, random numbers for x and y positions are generated in each pseudo-rapidity range until the number of the entries in each pseudo-rapidity range reaches the number of charged-particles shown in Figure 15, as shown in Figure 16. In this calculation, the pseudo-rapidity range is $-3.5 < \eta < -2.5$, while the actual range is $-3.6 < \eta < -2.45$.

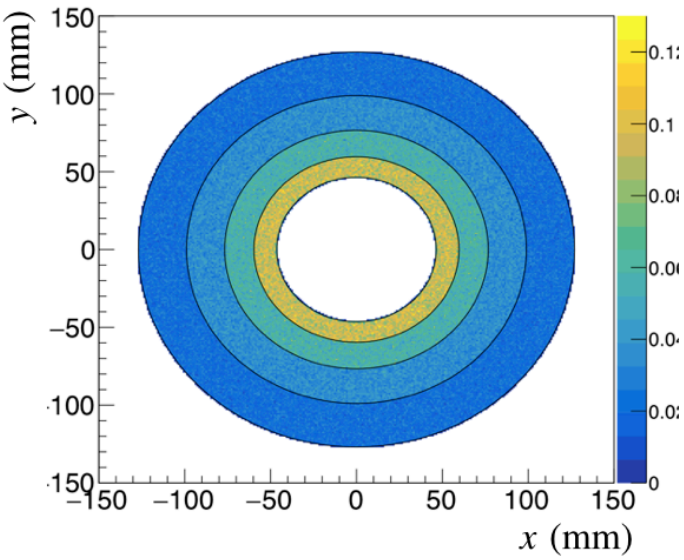

Figure 16: Charged-particle density at the last MFT plane estimated by Figure 15. Pseudo rapidity range is $-3.5 < \eta < -2.5$.

3.2.2 Multiple scattering effect [15]

A charged particle traversing a medium is deflected by many small-angle scatters. This phenomenon is called multiple scattering. Most of the deflection is due to Coulomb scattering from nuclei. The standard deviation of the angular distribution θ_0 and the position distribution x_0 after charged particles transversing a medium can be calculated as:

$$\theta_0 = \frac{13.6 \text{ MeV}}{\beta cp} z \sqrt{\frac{L}{X_0}} \left[1 + 0.038 \ln\left(\frac{L}{X_0}\right)\right] \tag{2}$$

$$x_0 = \frac{1}{\sqrt{3}} L\theta_0 \tag{3}$$

where p is momentum, βc is velocity, z is charge number of the injected particle, and L is the length of the medium. β can be calculated as:

$$\beta = \frac{p}{E} = \frac{p}{\sqrt{p^2 + m^2}} \tag{4}$$

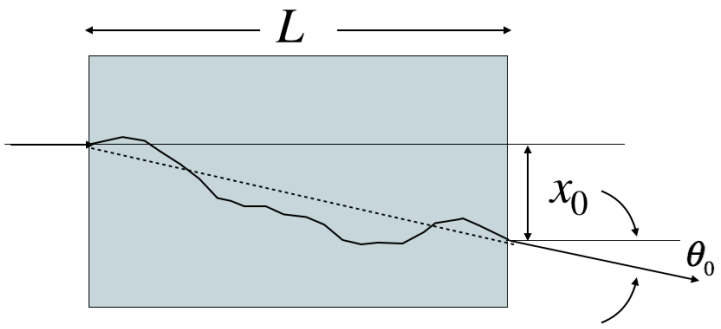

Figure 17: Schematic drawing of multiple scattering.

Table 4 summaries the assigned values for multiple scattering calculations to get values after a muon traverses the absorber.

Table 4: Assigned values for multiple scattering calculations

Variable	Assigned value
muon mass m	106 (MeV/c^2)
charge number z	-1
length of medium L	4.13 (m) = $60X_0$

Figure 18 shows the standard deviation of angular distribution θ_0 and position distribution x_0 as a function of transverse momentum p_T respectively when a muon transverses the hadron absorber.

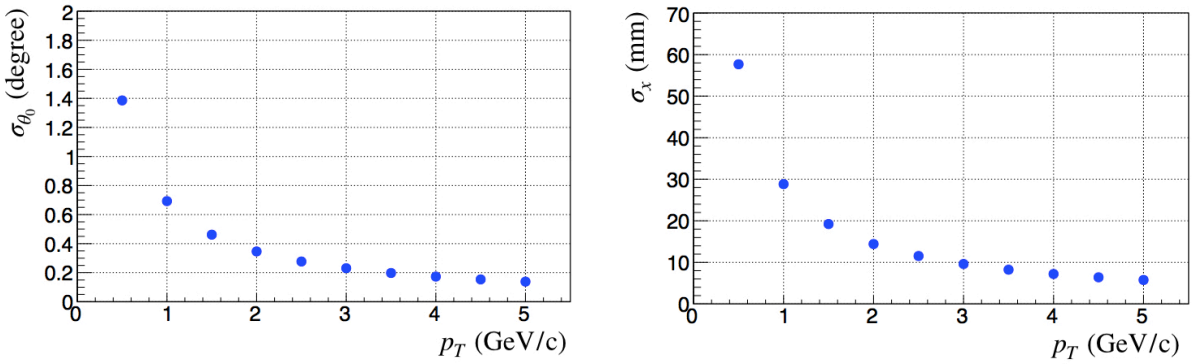

Figure 18: (left) Standard deviation of angular distribution as a function of muon transverse momentum. (right) Standard deviation of position distribution as a function of muon transverse momentum.

3.2.3 Number of MFT track candidates

Figure 19 shows the number of MFT track candidates determined by multiple scattering at $\eta = 3$ of the last MFT plane in 0-5% central Pb-Pb collision at $\sqrt{s_{NN}} = 5.02$ TeV as a function of p_T obtained from equation 1. The number of injected particles per unit area at $\eta = 3$ of the last MFT plane is $\sigma_{\eta=3} = 0.049$ (mm^{-2}) is calculated in Section 3.2.1.

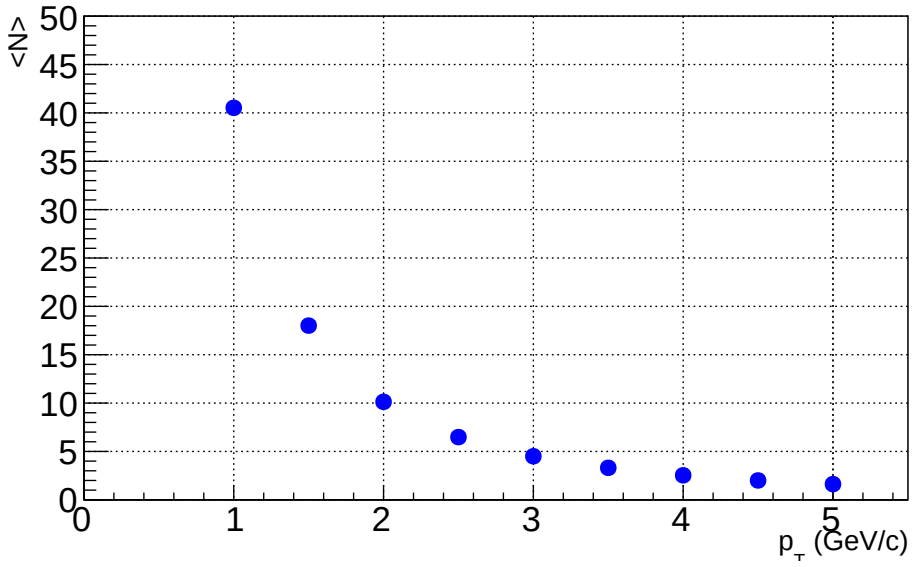

Figure 19: The number of MFT track candidates determined by multiple scattering at $\eta = 3$ of the last MFT plane in 0-5% central Pb-Pb collision at $\sqrt{s_{NN}} = 5.02$ as a function of p_T obtained from equation 1

For example, when the muon is $p_T = 1$ GeV/c, the number of MFT track candidates determined by multiple scattering are calculated as:

$$\begin{aligned} < N > &= \sigma_{\eta=3} * h_x * h_y \\ &= 0.049 \text{ (mm}^{-2}) * 28.8 \text{ (mm)} * 28.8 \text{ (mm)} \\ &\sim 41 \end{aligned} \tag{5}$$

There are approximately 41 MFT track candidates for one MUON track at $p_T = 1$ GeV/c. The number of MFT track candidates determined by multiple scattering is too large to connect to one MUON track. Therefore we develop the matching method using the correlation between track position and angle to reduce the number of MFT track candidates.

3.3 Development of matching method with the correlation between track position and angle

3.3.1 Correlation between track position and angle

Most MFT track candidates are the background that does not match with the MUON track. The background is reduced by the correlation between track position and angle. The muon passing through the absorber from left to right in Figure 20 has a probability distribution of the position and angle at the entrance of the absorber.

Figure 20: Schematic of muon passing through the absorber.

For example, suppose there is a muon that passes $x = 0$ at the end of the absorber ($z = -5.03$ m) as shown by the black arrow in Figure 21 (right). When the muon enters the absorber from a higher/(lower) position, it should have a smaller/(bigger) angle at the entrance of the absorber ($z = -0.9$ m) to connect to the muon that is $x = 0$ at the exit of the absorber. The illustration of the distribution of the position and angle at the entrance of the absorber for the muon that passes through $x = 0$ at the exit of the absorber is shown in Figure 21 (left). Each standard deviation of the probability distribution should be equivalent to the calculated values by the equation (2) and (3). The standard deviation of the position distribution shown by hx in Figure 21 (left) is the search window determined by multiple scattering.

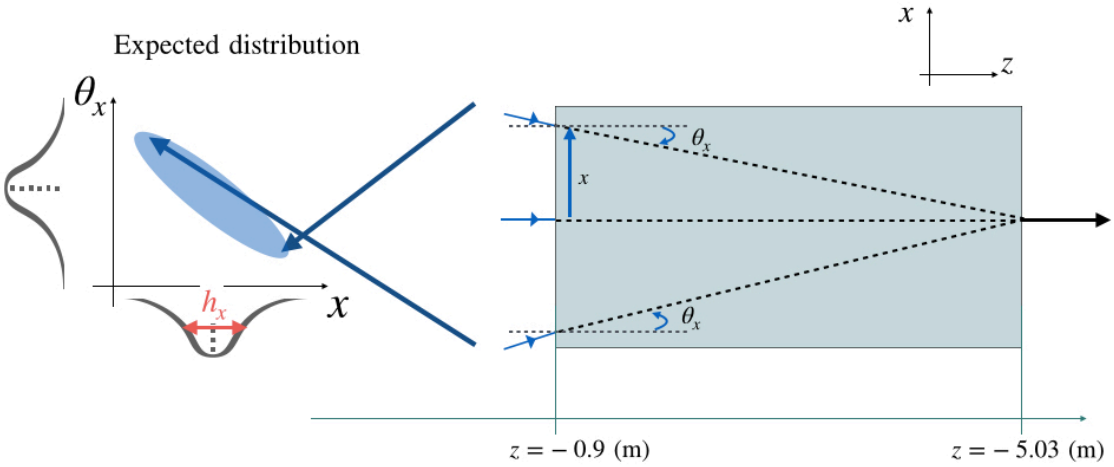

Figure 21: (left) Illustration of the expected distribution of the position and angle at the entrance of the absorber for the muon that is $x = 0$ at the exit of the absorber. (right) Schematic illustration of the muon passing through the absorber.

The muons that originate only near the vertex need to be considered as a signal track from the collisions. Red arrows in Figure 22 (right) shows the muons that originate near the vertex. When the particles fly from the vertex towards the entrance of the absorber

($z = -0.9$ m), the position x, y and angle θ_x, θ_y of the particles at the entrance of the absorber shown by the red line in Figure 22 (left) are calculated as:

$$\theta_x = ax \tag{6}$$

where a is the slope that is calculated from the distance between the collision point and absorber. When the collision point is $Z = 0.0$ (m), the position x, y and angle θ_x, θ_y of the particles at the entrance of the absorber are calculated as:

$$\theta_x = 0.063x \tag{7}$$

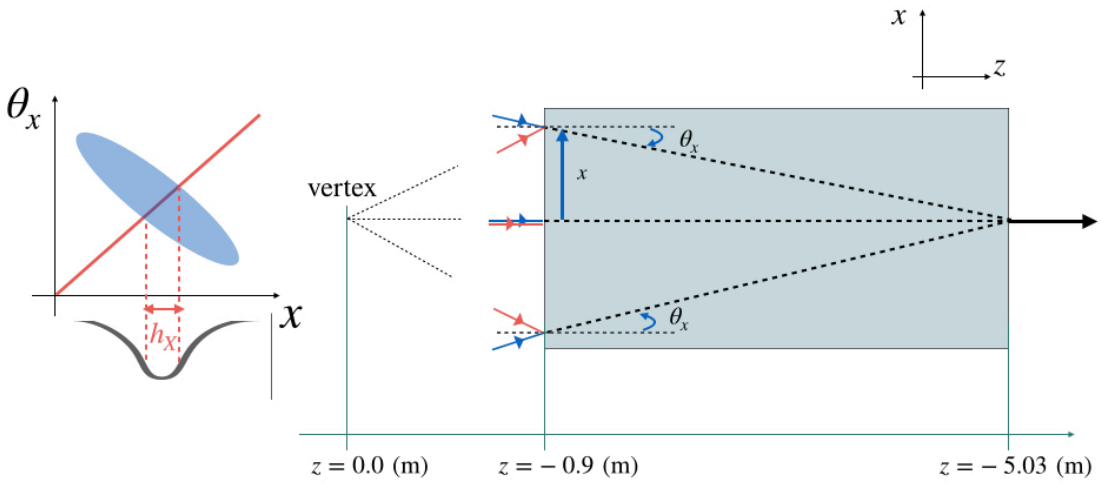

Figure 22: (left) Red line indicating a possible association of the position and angle for tracks that originate near the vertex. Expected distribution of the position and angle at the entrance of the absorber for the muon that is $x = 0$ at the exit of the absorber. (right) Schematic of the muon passing through the absorber.

In this example, tracks need to satisfy the two conditions. First is tracks come from the vertex. Second is tracks pass the end of the absorber at $x = 0$ with 0 degree. Then, the overlap range of the red line and the blue distribution becomes the new search window shown by hx in Figure 22 (left).

3.3.2 Geant4 simulation setup

To get a correlation distribution of the track position and angle, Geant4 simulation is carried out. Geant4 is a toolkit for the simulation of the passage of particles through matter using Monte Carlo methods. Its application area includes high energy, nuclear and accelerator physics, space science, and medical studies. [16], [17]

In this simulation, an absorber that has the same length and material budget as the hadron absorber of MUON (Table 1) is used. Particles go through the absorber from

the carbon side ($z = -0.9$ m) to the steel side ($z = -5.03$ m) in a real experimental situation. However, to make the simulation easier, muons are injected from the steel side ($z = -5.03$ m) towards the vertex ($z = 0.0$ m) in this simulation. Confirmation of this simulation method by another simulation to confirm that the output has the same tendency regardless of the incident direction, is summarized in Section 3.3.4.

Figure 23 shows the variables used in the simulation. Since the pseudo-rapidity range of the MFT is $-3.6 < \eta < -2.45$ and $\eta = -3$ is almost at the center of the MFT, the muon is injected at $\eta = -3$ from the steel side of the absorber toward the vertex. $\eta = -3$ corresponds to an approximate angle of 5.7°. Incident position is set to $x_{MUON} = 0.501$ (m) to be able to reach the vertex. Table 5 summaries the assigned values in the simulation.

When muons reach the boundary between carbon and vacuum ($z = -0.9$ m), track positions x_{MFT} and angles θ_{MFT} are recorded. Track positions and angles are not recorded when muons decayed in the absorber and then other kinds of particles reached the boundary between carbon and vacuum.

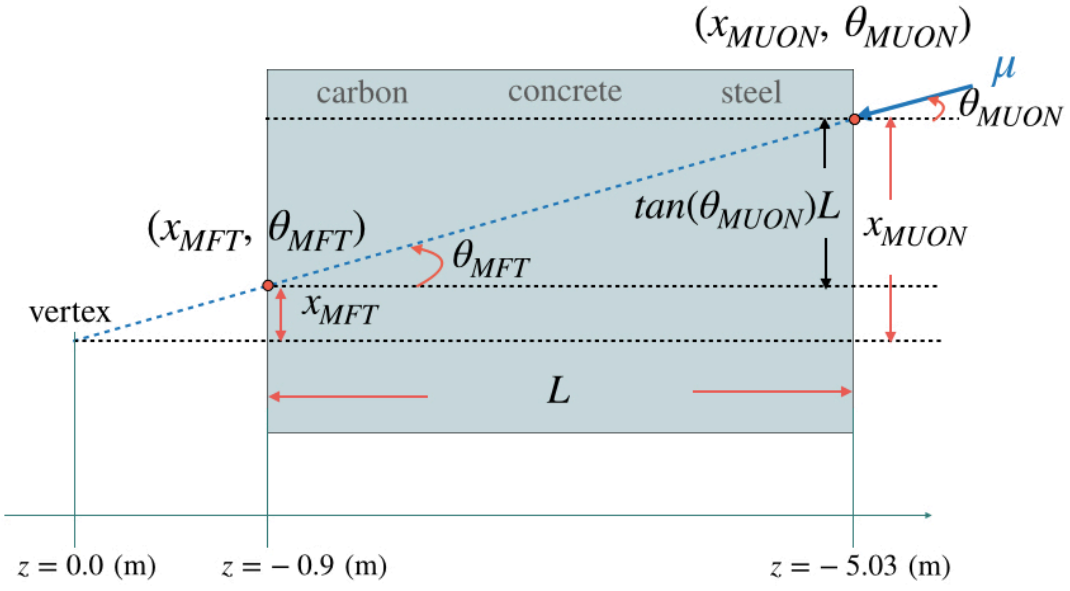

Figure 23: Schematic drawing of the Geant4 simulation setup

Table 5: Assigned values in the Geant4 simulation

Variable	Assigned value
Incident position of z-axis	-5.02 (m)
Incident position of x-axis x_{MUON}	0.501 (m)
Incident angle θ_{MUON}	5.7°

Figure 24 shows the event display of Geant4 simulation for an event. The red line indicates a negative charge, the blue line indicates a positive charge, and the green line indicates a neutral charge. The red line that penetrates the absorber is the incident muon.

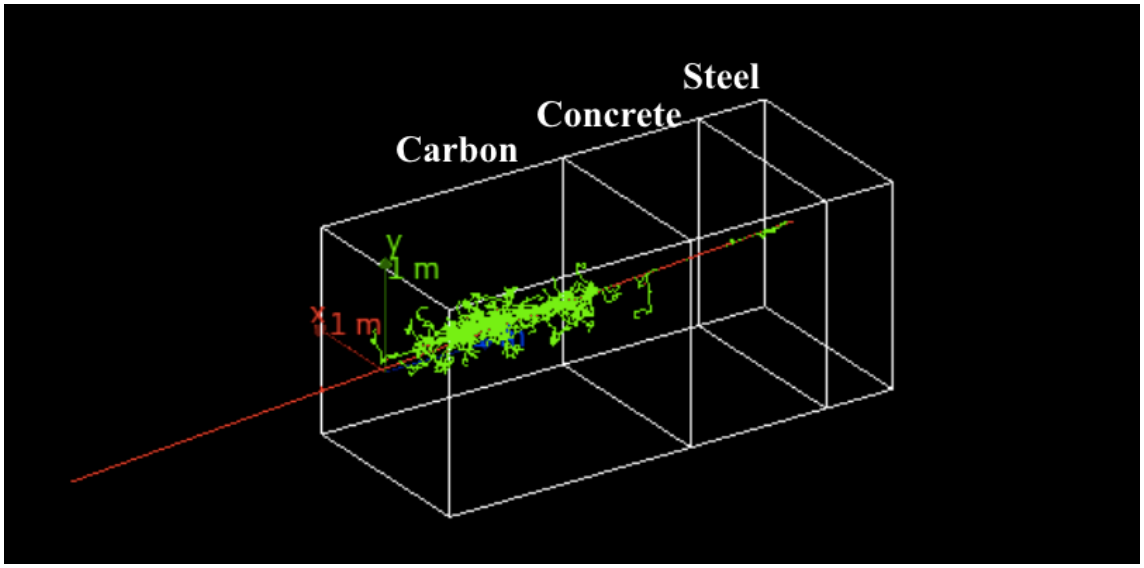

Figure 24: Event display of Geant4 simulation. Muon is injected from steel side at $\eta = 3$ ($\theta \sim 5.7°$) towards the vertex ($z = 0$ m).

Figure 25 shows the correlation distribution of the position x_{MFT} and angle θ_{MFT} of $p_T = 1$ GeV/c and $p_T = 2$ GeV/c. The mean value of the angle $\overline{\theta_{MFT}} \sim 5.7$ and the position $\overline{x_{MFT}} \sim 89.8$ indicate most muons went through the absorber straightly. Table 6 shows the comparison of the standard deviation between the simulation and the multiple scattering calculation by equation (2) and (3) in Section 3.2.2 when $p_T = 1$ GeV/c. The standard deviation of the angle is almost same in the simulation and calculation, while the standard deviation of the position is different since there is no material information of the absorber in the calculation.

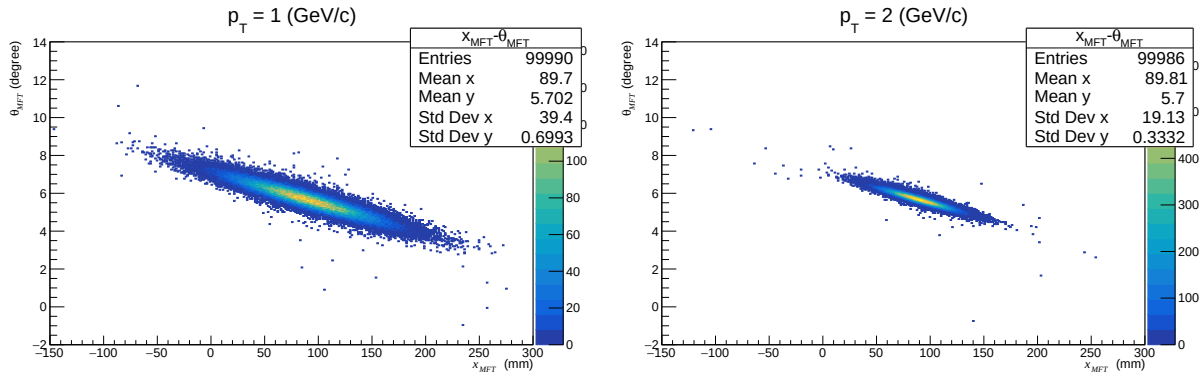

Figure 25: Correlation distribution of the position and angle of transverse momentum $p_T = 1$ GeV/c (left) and $p_T = 2$ GeV/c (right).

Table 6: Comparison of the standard deviation between the simulation and the multiple scattering calculation (Section 3.2.2) at $p_T = 1$ GeV/c.

	σ_x	σ_θ
Simulation	39.4	0.6993
Caluculation	28.8	0.6927

3.3.3 Number of candidates determined by correlation

Figure 26 shows the correlation distribution of the position and angle of $p_T = 1$ GeV simulated by Geant4, and the red line indicating the correlation between the position and angle at the left side of the absorber ($z = -0.9$ m) of tracks that originate near the vertex. Each elliptical line above the correlation distribution indicates efficiency. Efficiency is defined as the percentage of entries inside the ellipse. Overlap region of the red line and each efficiency line are defined as the search window. There is a respective percentage of entries in each efficiency line. Efficiency cut is applied to both x and y directions. Efficiency cuts of x and y directions are defined as ϵ_x and ϵ_y.

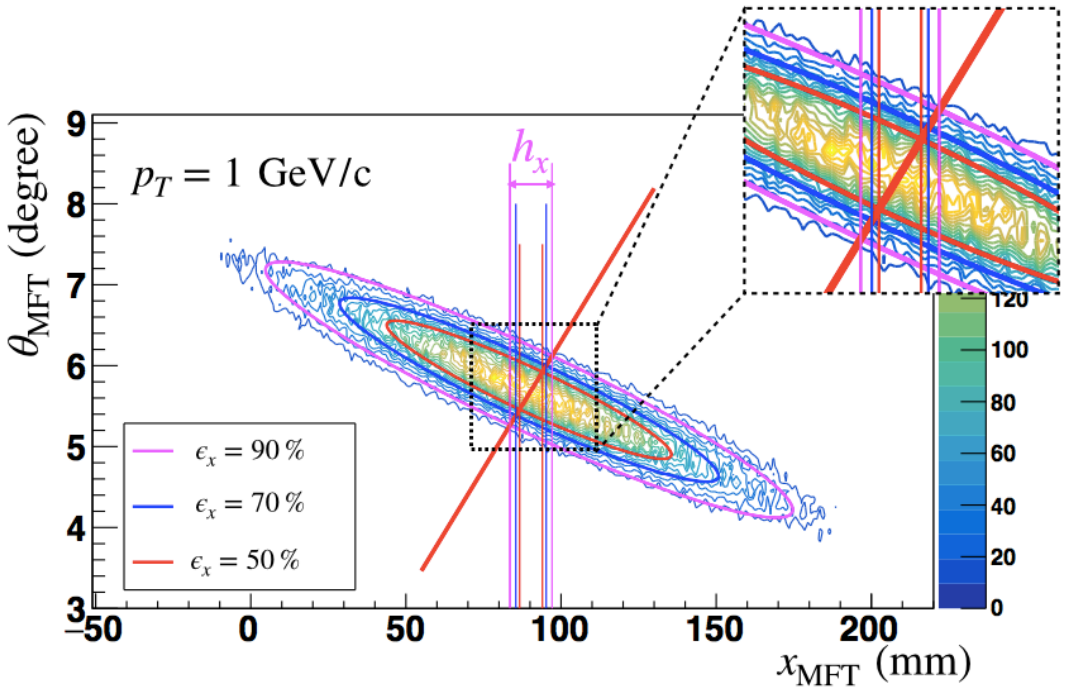

Figure 26: Correlation distribution of the position and angle of transverse momentum $p_T = 1$ GeV/c simulated by Geant4. The red straight line indicating the correlation between the position and angle at the left side of the absorber ($z = -0.9$ m) of tracks that originate near the vertex. Each elliptical line above the correlation distribution indicates efficiency. Overlap region of the red line and each efficiency line are defined as the search window.

Two-dimensional efficiency cut ϵ_{xy} is defined as:

$$\epsilon_{xy} = \epsilon_x * \epsilon_y \tag{8}$$

Figure 27 shows a one-dimensional search window determined by the correlation distribution of the position and angle as a function of p_T.

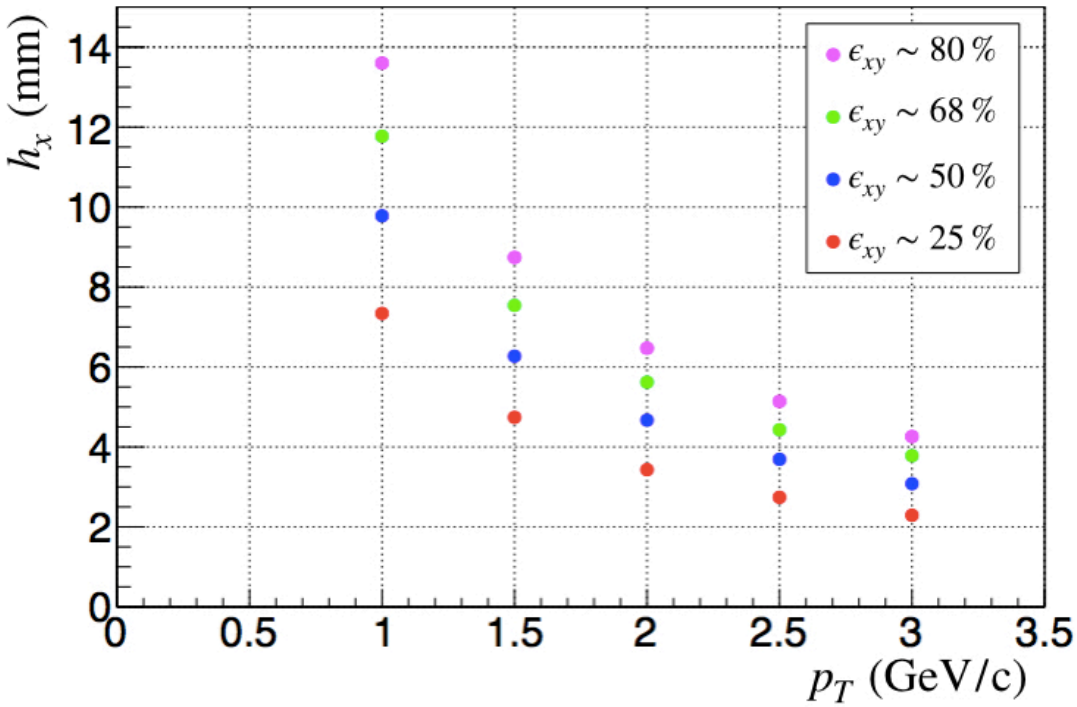

Figure 27: One dimensional search window determined by the correlation distribution of the position and angle as a function of p_T.

The number of candidates $< N >$ at arbitrary pseudo-rapidity is calculated from equation (1). Figure 28 shows the number of MFT track candidates after background subtraction by the correlation between track position and angle at $\eta = 3$ of the last MFT plane in 0-5% central Pb-Pb collision at $\sqrt{s_{NN}} = 5.02$ TeV as a function of p_T obtained from equation (1).

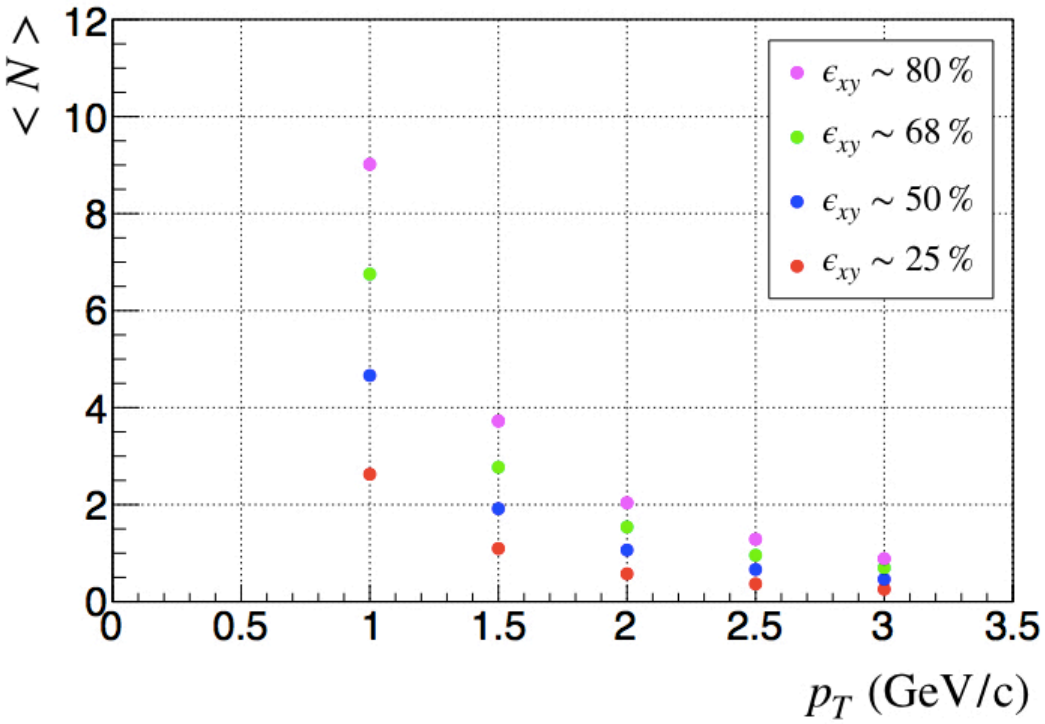

Figure 28: The number of MFT track candidates at $\eta = 3$ of the last MFT plane in 0-5% central Pb-Pb collision at $\sqrt{s_{NN}} = 5.02$ TeV as a function of p_T obtained from equation 1.

For example, when MUON track is $p_T = 1$ GeV/c and two-dimensional efficiency cut is $\epsilon_{xy} \sim 68\%$, the number of MFT track candidates after background subtraction by the correlation between track position and angle are calculated as:

$$\begin{aligned} < N > &= \sigma_{\eta=3} * h_x * h_y \\ &= 0.049 \ (\mathrm{mm}^{-2}) * 11.8 \ (\mathrm{mm}) * 11.8 \ (\mathrm{mm}) \\ &\sim 6.8. \end{aligned} \tag{9}$$

There are approximately 6.8 MFT track candidates after background subtraction by the correlation between track position and angle, while there are approximately 41 MFT track candidates before background subtraction (equation (5)). Background can be significantly reduced about 6 times. Figure 29 shows a comparison of the number of MFT track candidates between before and after background subtraction. Furthermore, the background can be reduced by the sign of charged particle and rough momentum matching between MFT and MUON.

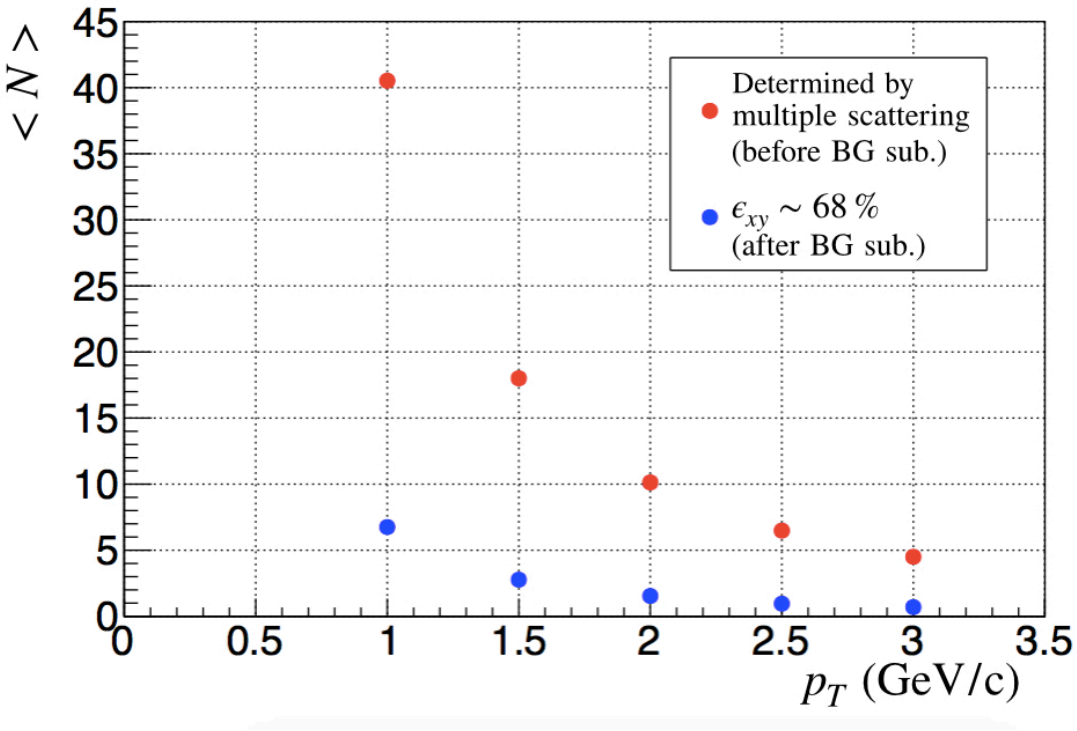

Figure 29: Comparison of the number of MFT track candidates before and after background subtraction. Red dot represents the number of candidates before background subtraction and blue dot represents after subtraction.

3.3.4 Confirmation of Geant4 simulation

In the Geant4 simulation in Section 3.3.2, muons are injected from the steel side ($z = -5.03$ m) towards the vertex ($z = 0.0$ m) to make the simulation easier, while particles go through the absorber from the carbon side ($z = -0.9$ m) to the steel side ($z = -5.03$ m) in a real experimental situation. In this section, another simulation to confirm the incident position does not affect the results is summarized.

In this simulation, an absorber that has approximately the same length (4 m) and material budget ($55X_0$) as the hadron absorber of MUON is used, as shown in Table 7.

Table 7: Geometrical parameters of the hadron absorber in the confirmation simulation

Material	Length (m)	Material budget
Carbon	220	18.8
Concrete	123	10.7
Steel	57	1.76
Total	400	-

The incident position of the z-axis is fixed at the vertex ($z = 0$ m) in this study. The incident position of the x-axis is changed from -20 mm to 160 mm by 1 mm. The incident angle is changed from 3.0° to 8.0° by 0.1°. In each position and angle, 100 muons are injected. When muon reaches the range around $\eta = -3$ at the exit of the absorber, the position x_{MFT} and angle θ_{MFT} on the entrance of the absorber are recorded. $\eta = -3$

corresponds to the approximate angle of 5.7°. When muon that angel is 5.7° reaches the end of the absorber, the position of the x-axis is 475.9 mm. Here, the range around $\eta = -3$ is defined as $470.9 < x < 480.9$ mm and $5.2° < \theta < 6.2°$. Figure 30 and Table 8 summarize the assigned parameters in the simulation. It is confirmed that the incident position does not affect the results.

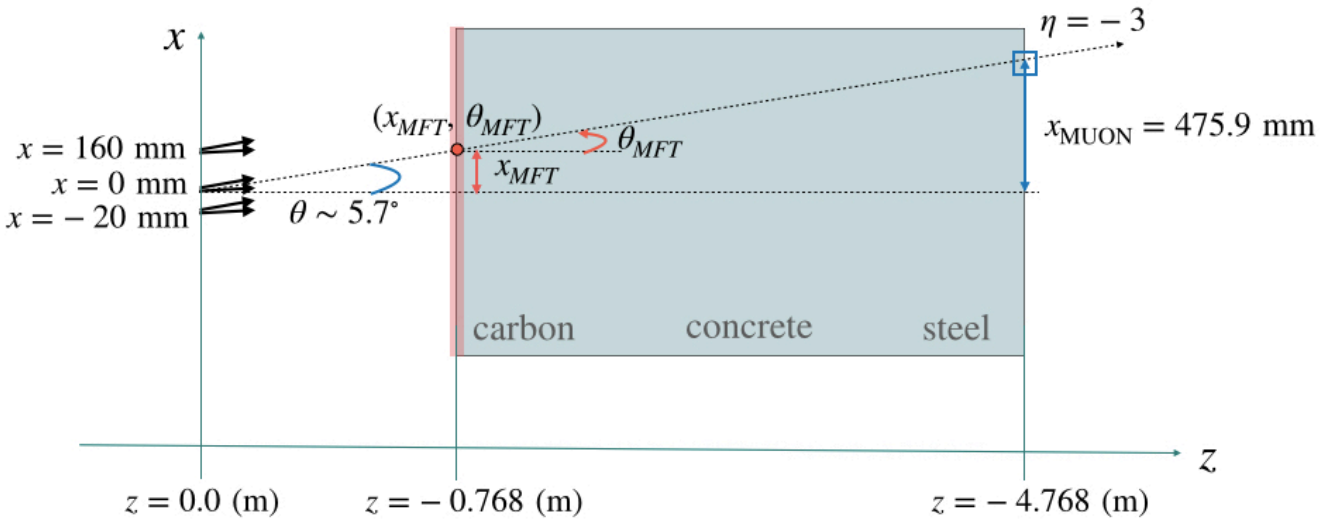

Figure 30: Schematic drawing of the confirmation simulation setup.

Table 8: Assigned parameters in the confirmation simulation.

Variable	Assigned parameters
Incident position of z-axis	0 (mm): fixed
Incident position of x-axis	-20<x<160 (mm): 1mm step
Incident angle	3.0°<θ<8.0°: 1° step

The left panel of Figure 31 left shows the correlation between the position and angle at the entrance of the absorber for muons that are injected from the exit of absorber towards the vertex at $\eta = -3$ (same situation as Section 3.2.2). The right panel of Figure 31 right shows the correlation between the position and angle at the entrance of the absorber for muons that reaches the range around $\eta = -3$ at the exit of the absorber. The functions of the ellipses drawn in the same colors are the same in both figures. The percentage of entries in the ellipse is defined as efficiency. Efficiency lines $(90, 70, 50\%)$ defined in left figure give consistent results $(88, 68, 47\%)$ in right figure.

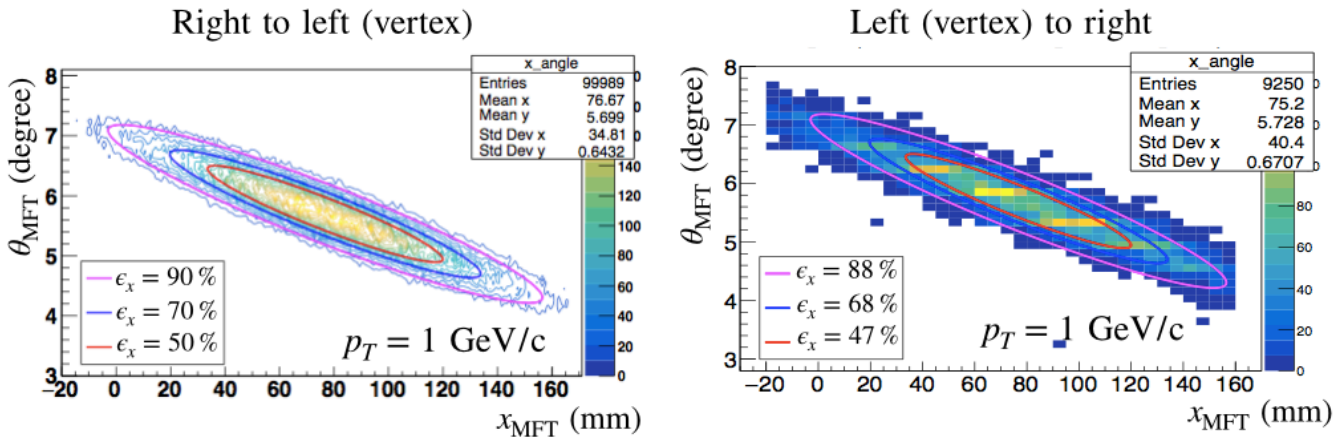

Figure 31: (left) Correlation between the position and angle at the entrance of the absorber for muon that is injected from the exit of absorber towards the vertex at $\eta = -3$ (same situation as 3.2.2). (right) Correlation between the position and angle at the entrance of the absorber for muons that reached the range around pseudo-rapidity $\eta = -3$ at the exit of the absorber.

3.4 Preparation for evaluation of matching algorithm

To select the best MFT track from the MFT track candidates, the likelihood of the MFT track candidates is evaluated by the following factors. That is the correlation between the track position and angle, and momentum and charged sign matching between MFT and MUON. The new matching method simulated in Section 3.2.2 needs to be implemented in the matching algorithm.

Steps to implement the new matching method are summarized below. First, correlation distribution can be obtained from the MUON track. The size of the distribution depends on the MUON track momentum. Second, the MFT track that is the nearest to the center of the distribution is the best MFT track. To calculate the distance from the center of the ellipse is harder than calculating the distance from the center of the circle. In order to make analysis easier, elliptical distribution given in Section 3.2.2 is converted to circular distribution.

Figure 32 shows the process to convert the elliptical distribution to circular distribution that center is zero. Each process is shown below. The step numbers are corresponding to the numbers of the panel in Figure 32.

1. The original correlation distribution of the track position and angle at $p_T = 1$ GeV/c simulated by Geant4. This is the same figure as Figure 26.
2. The center of Figure 32-1 is converted to zero. Each axis is converted by equation (10) and (11).

$$x_2 = (x_{MUON} - x_{MFT}) - tan\left(\frac{\theta_{MFT} + \theta_{MUON}}{2}\right)/L \tag{10}$$

$$y_2 = \theta_{MUON} - \theta_{MFT}. \tag{11}$$

3. The y-axis in Figure 32-2 is multiplied by $L/3$ to make the dimension the same as the x-axis and to make the distribution slope 45 degrees. $L/3$ is empirically found out.

4. Figure 32-3 is rotated 45 degrees to align the major axis of the ellipse with the x-axis.

5. Figure 32-4 is converted ellipse to a circle by dividing each x and y value by each standard deviation. Each standard deviation is obtained from the fit values of Figure 33.

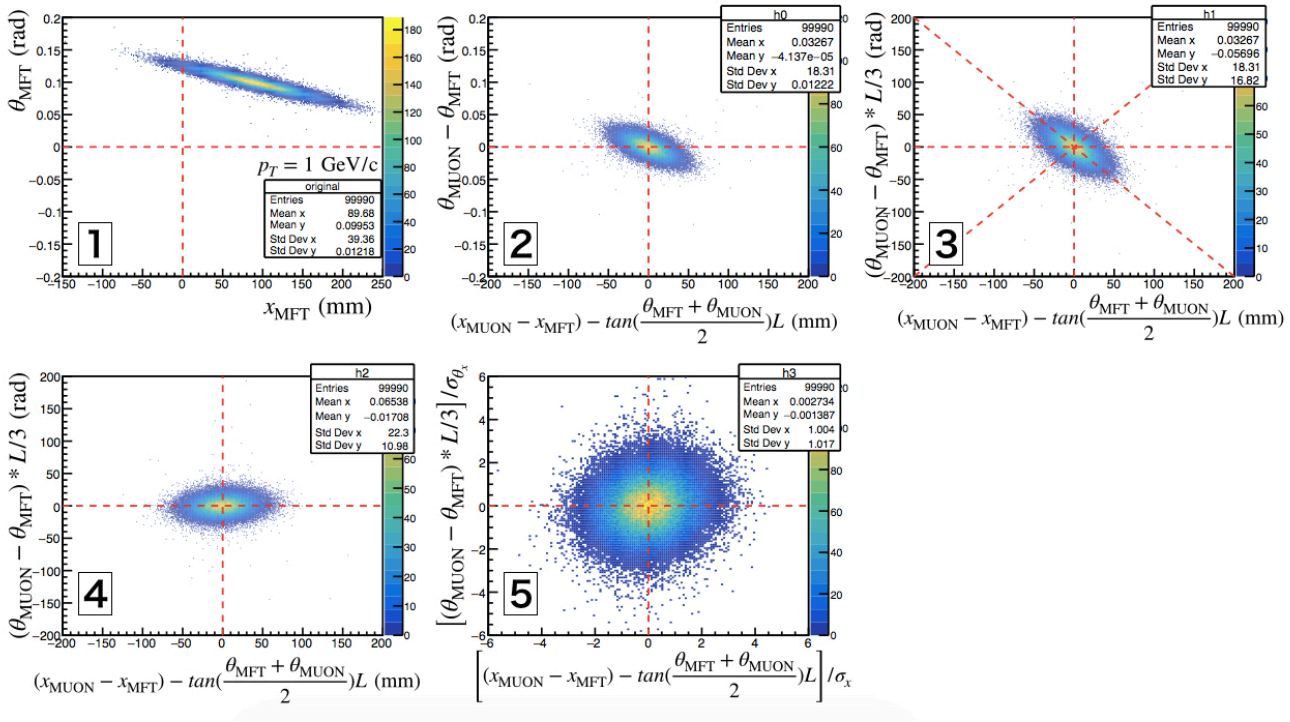

Figure 32: Process to convert the elliptical distribution to circular distribution that center is zero.

The left (right) panel of Figure 33 shows a projection of Figure 32-4 onto the x-axis (y-axis), respectively. Each histogram is fit by Gaussian function. The same processes are done for other p_T. Figure 34 shows standard deviations σ_x and σ_{θ_x} in Figure 32-4 as a function of p_T. The standard deviations vs. p_T is fit by function (12).

$$\sigma = A_1/p_T + A_2/p_T^2 \tag{12}$$

where A_1 and A_2 are fit parameters. Equation (13) is obtained as the result of fitting. Standard deviation in step 4 at certain p_T can be calculated by equation (13).

$$\sigma_x = 20.84/p_T + 1.349/p_T^2$$
$$\sigma_{\theta_x} = 8.603/p_T + 2.072/p_T^2 \tag{13}$$

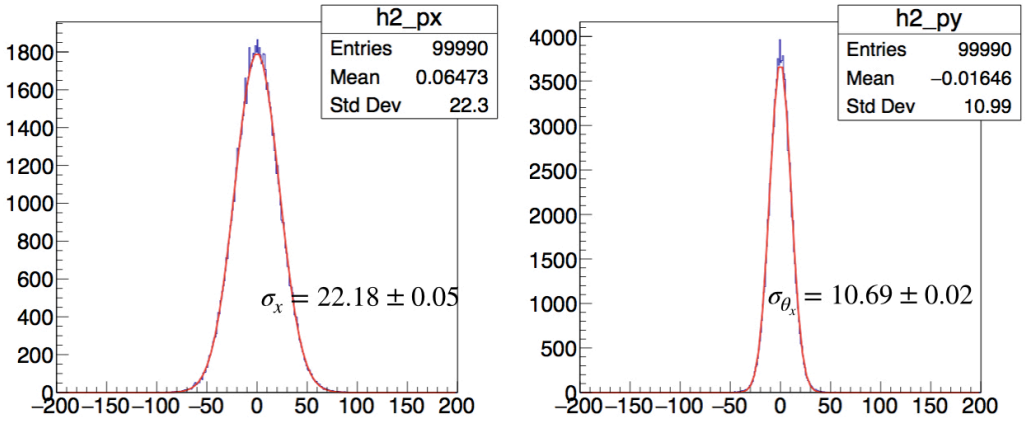

Figure 33: Projection of Figure 33-4 onto the x-axis (left) and y-axis (right), respectively. Each histogram is fit by Gaussian function.

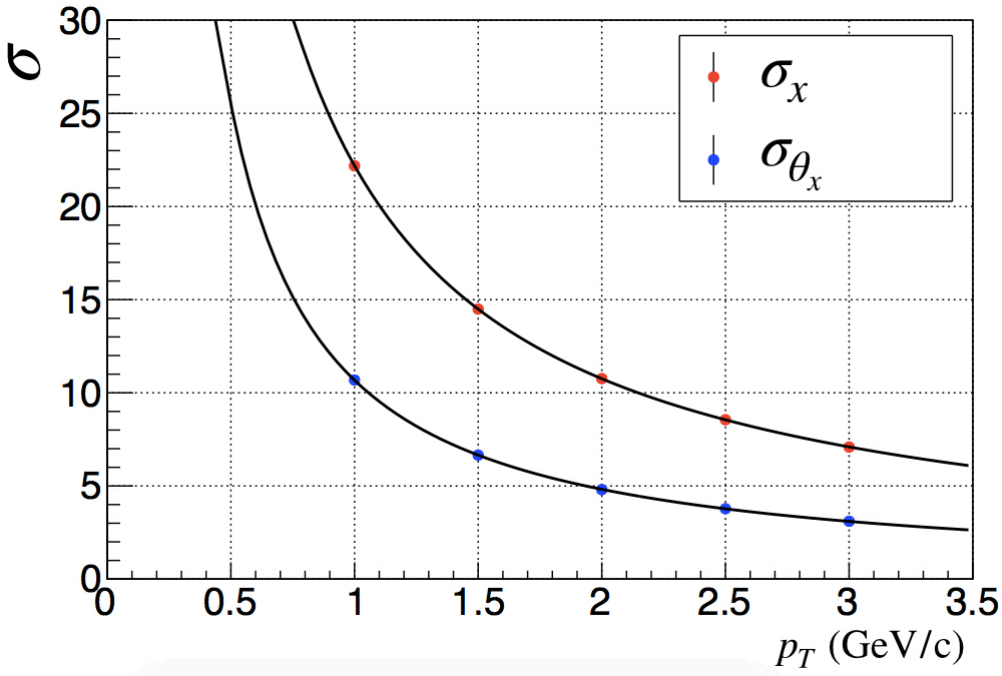

Figure 34: Standard deviation σ_x and σ_{θ_x} in step 4 as a function of p_T. Each standard deviation is obtained from the fit values of Figure 33.

Figure 35 (left) shows the original distributions and Figure 35 (right) shows the distributions after conversion with the efficiency lines. The upper (lower) panel of Figure 35

is $p_T = 1$ GeV ($p_T = 2$ GeV). The efficiency lines are defined as the percentage of entries inside ellipse or circle. The size of the original distribution depends on p_T, while the size of the distribution after all conversions described above does not depend on p_T. Figure 36 shows the percentage of entries in the right panel of Figure 35 as a function of radius r. r is defined as the distance from the center of the circular distribution after all conversion. Different color dots represent different p_T. All dots almost overlap. That is contour lines of efficiency can be written regardless of p_T. Therefore the MFT track that has smaller r is more likely to be the best MFT track regardless of p_T.

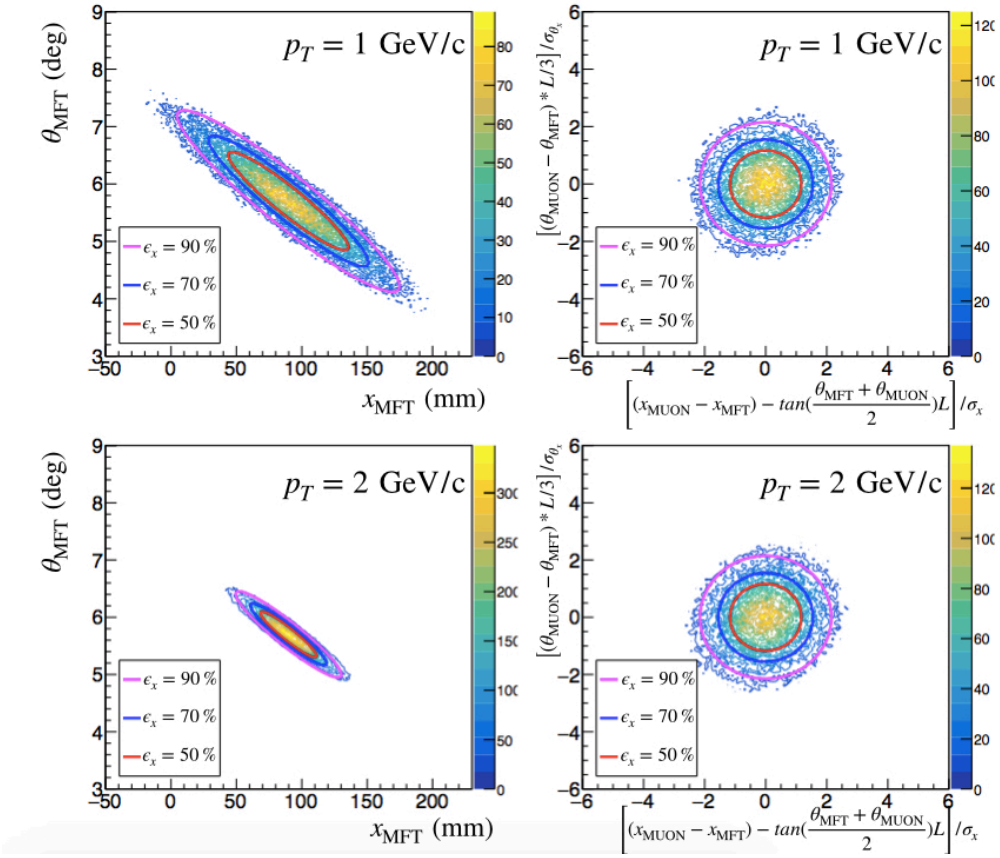

Figure 35: Original distributions (left) and distributions after conversion (right) with efficiency lines. The upper (lower) panel is $p_T = 1$ GeV ($p_T = 2$ GeV). Contour lines of efficiency can be written regardless of transverse momentum.

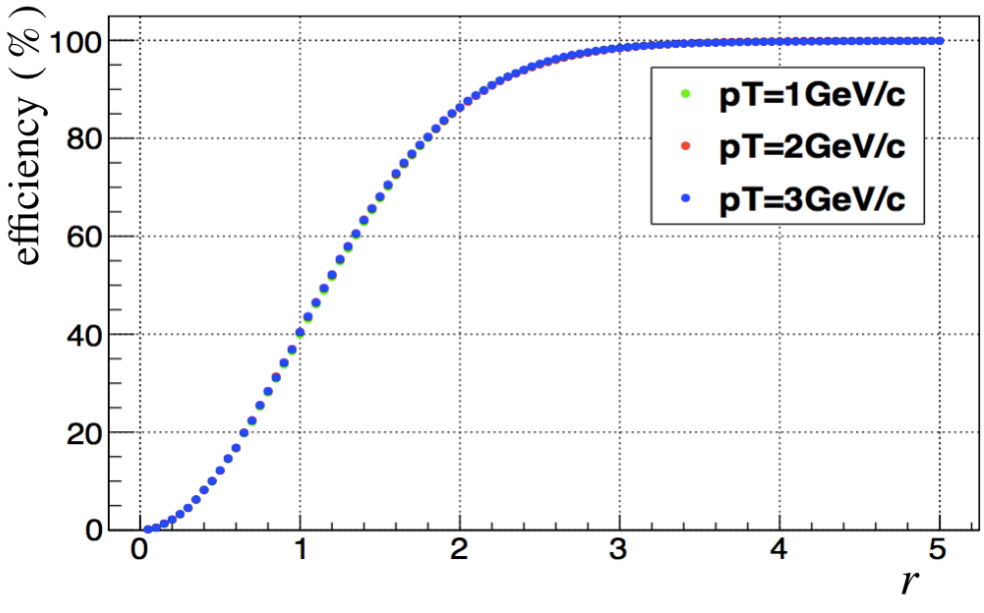

Figure 36: Percentage of entries in the right panel of Figure 35 as a function of radius r. Different color dots indicate different p_T.

4 Evaluation of developed matching algorithm

The developed matching algorithm is evaluated using HIJING [18].

4.1 Simulation tool for Heavy Ion Collisions

HIJING (Heavy Ion Jet INteraction Generator) is a Monte Carlo event generator particle production in high energy nuclear collisions. After HIJING generates particles emitted by high energy nuclear collisions, GEANT4 is used to simulate detector responses. In Monte Carlo simulation, we can know the true information of the particles in the events such as the particle ID, interaction points, momentum vector, and their mother particles. Therefore we can verify how well the developed matching algorithm performs to evaluate track candidates.

4.2 Evaluation setup

In this evaluation, central Pb-Pb collision in centrality 0-5% at $\sqrt{s_{NN}} = 5.5$ TeV is generated by HIJING and single muon that ϕ range is $0° < \phi < 360°$ is embedded at $\eta = -3$ for each event. Tracks generated by HIJING are the background in the evaluation. Detector responses are simulated by GEANT4. 30 events are simulated for each p_T ($p_T = 1, 2, 3$ GeV). Each MFT hit at the last MFT disk is scored for the MUON hit of the embedded single muon by calculating matching quality parameters. The matching quality parameters in the x and y directions r_x and r_y are defined as:

$$r_x = \sqrt{x'^2 + \theta'^2_x} \tag{14}$$

$$r_y = \sqrt{y'^2 + \theta'^2_y} \tag{15}$$

where $x^{'}, \theta^{'}_x, y^{'}, \theta^{'}_y$ are the values after the conversion from elliptical to circular distribution in Section 3.4. They are calculated as:

$$x^{'} = \left[(x_{MUON} - x_{MFT}) - tan\left(\frac{\theta_{MFT} + \theta_{MUON}}{2} \right) / L \right] / \sigma_x \tag{16}$$

$$\theta^{'}_x = \left[(\theta_{MUON} - \theta_{MFT}) * L/3 \right] / \sigma_{\theta_x} \tag{17}$$

$$y^{'} = \left[(y_{MUON} - y_{MFT}) - tan\left(\frac{\theta_{MFT} + \theta_{MUON}}{2} \right) / L \right] / \sigma_y \tag{18}$$

$$\theta^{'}_y = \left[(\theta_{MUON} - \theta_{MFT}) * L/3 \right] / \sigma_{\theta_y} \tag{19}$$

The r_x (r_y) is the distance from the center of the 2 dimensional histogram (θ_x (θ_y) vs. $x^{'}$ ($y^{'}$)) that is the circular distribution as shown in the right pannel of Figure 35. The track that have the smallest r_x or r_y is chosen as the best MFT track in each direction. r_x and r_y are the one-dimensional matching quality parameters. Two-dimensional matching quality parameter R considering both r_x and r_y is defined as:

$$\begin{aligned} R &= r_x + r_y \\ &= \sqrt{x'^2 + \theta_x'^2 + y'^2 + \theta_y'^2}. \end{aligned} \tag{20}$$

The track that has the smallest R among the track candidates is chosen as the best MFT track. Since this is a simulation, we can check which track is a single muon in the MFT track candidates. Therefore, when we arrange R in ascending order, we can get the ranking of how small R of the embedded muon is among all entries. In this simulation, true positions and momentum vectors from simulated information not reconstructed information are used at the last MFT disk and the first MUON tracking chamber.

4.3 Result

Figure 37 shows the distribution of track position and angle in the x-direction for 10 events on the last MFT plane. The center of the distribution is $(0, 0)$ and most of the hit points are on the linear line. Distributions have a similar tendency regardless of p_T of the signal (embedded single muon). The distribution of the position and angle for y-direction has the same tendency as x-direction. Figure 38 shows the distribution of the normalized position $x^{'}$ and angle $\theta_x^{'}$. The distribution spreads as p_T of embedded single muon increases because $x^{'}$ and $\theta_x^{'}$ are normalized values by σ_x and σ_{θ_x} which depend on p_T of the signal (equation 16 and 17). The distribution of the normalized position $y^{'}$ and angle $\theta_y^{'}$ has the same tendency. Figure 39 shows the distribution of rx and ry. The distribution spreads as p_T of the signal increases because r_x and r_y are normalized values by σ_x, σ_{θ_x}, σ_y and σ_{θ_y} which depend on p_T of the signal (equation 14 to 19).

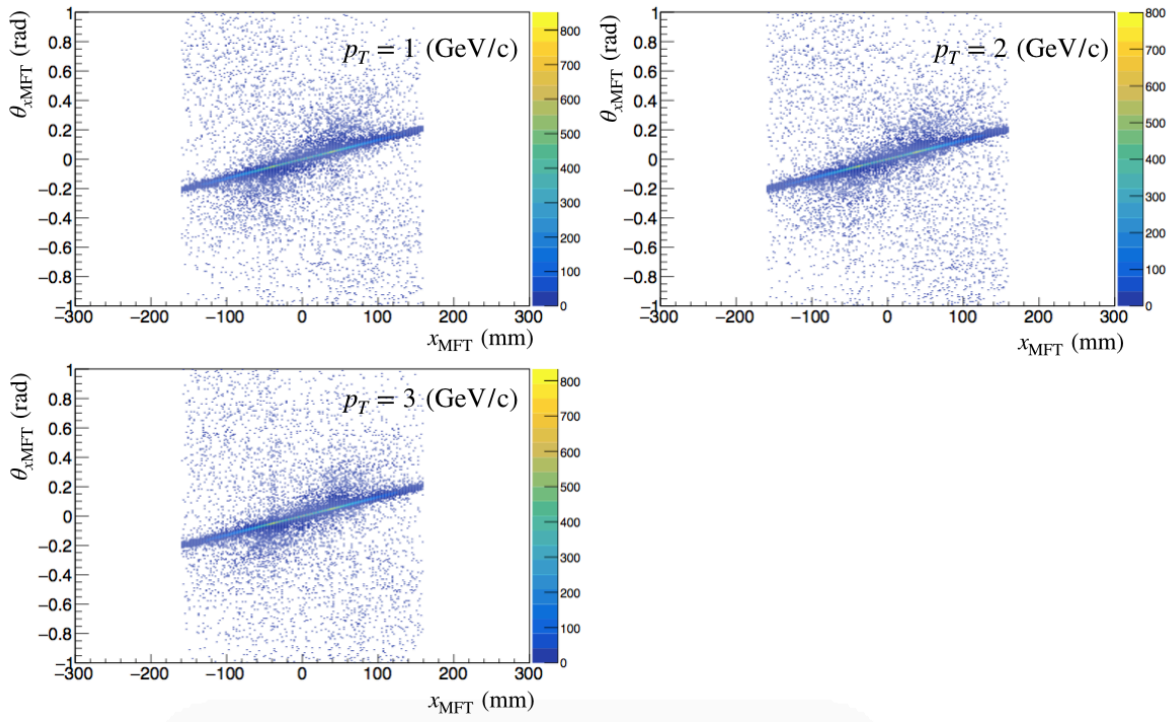

Figure 37: Distribution of the position and angle for x direction at the last MFT plane. p_T of embedded single muon is shown in each panel.

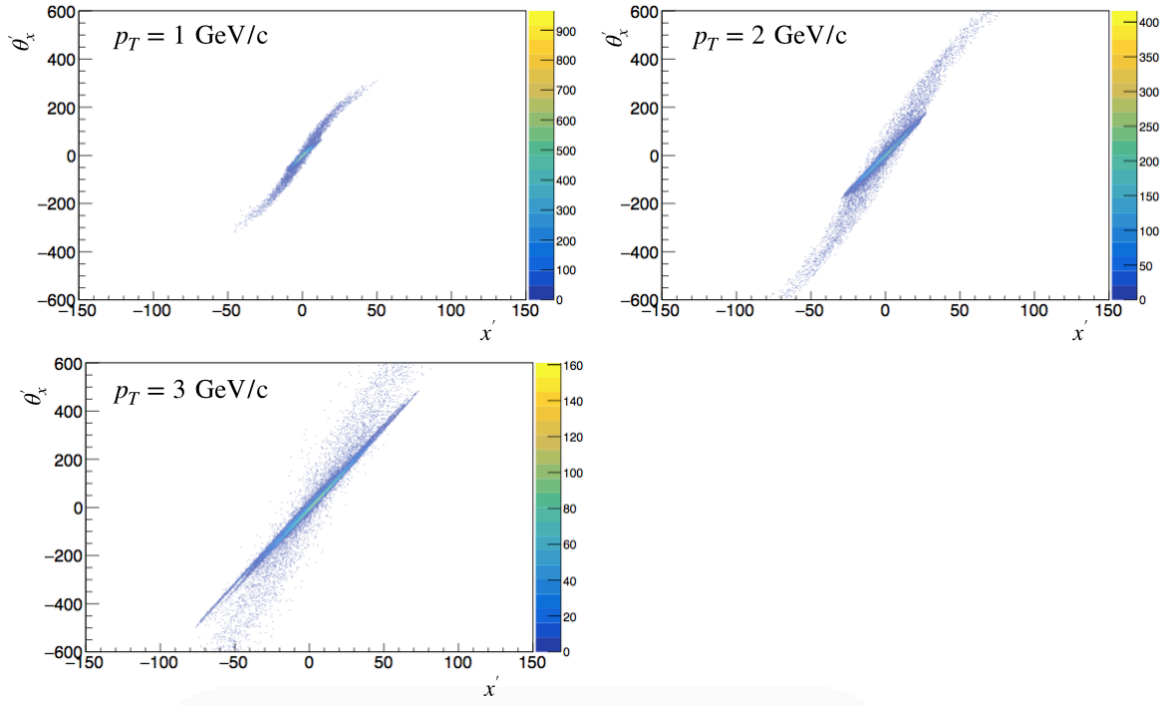

Figure 38: Distribution of the normalized position $x^{'}$ and angle $\theta^{'}_{x}$ for x direction. p_T of embedded single muon is shown in each panel.

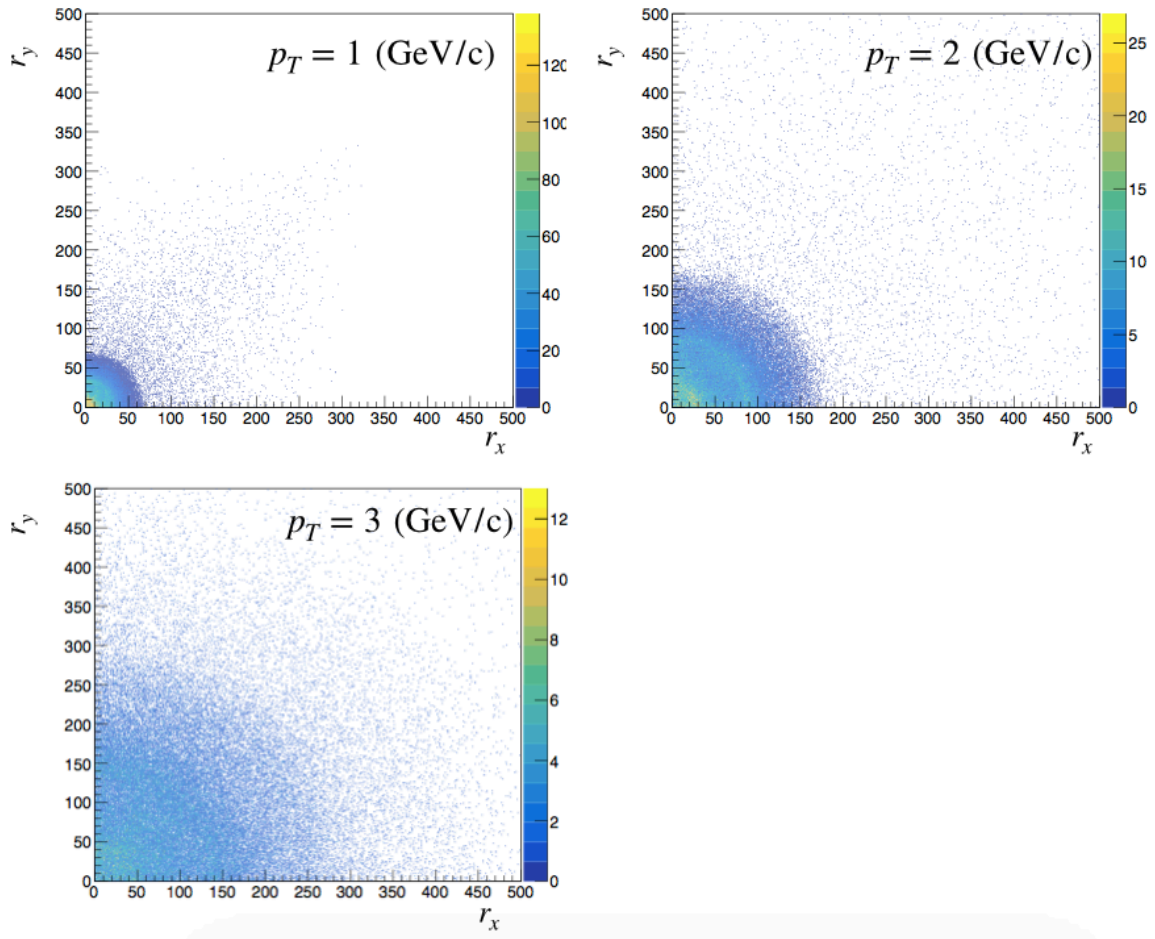

Figure 39: Distribution of rx and ry. p_T for embedded single muon is shown in each panel.

Figure 40, 41, 42 shows r_x, r_y and R respectively. Red line represents embedded muon and blue line represents background. The red line (embedded single muon) has a peak in a small region around from 0 to 3 mm, while the blue line (background) spreads evenly to large region for all r_x, r_y and R as expected. r_x and r_y have similar results. R, which combines the two of r_x and r_y, has a lower background ratio than r_x and r_y alone. R can reduce the amount of the background by almost an order of magnitude compared to r_x and r_y at any p_T, especially at low R. The ratio of background to signal decreases with increasing p_T especially for R as shown in Figure 42. Figure 43 shows R only for background. Peak position is smaller in lower p_T than higer p_T. R distribution is sharp in lower p_T, while R distribution is smooth in higer p_T This is because R is normalized value by the standard deviation which depends on p_T shown in Figure 34 and background before normalization is similar in any p_T. Therefore this affects the ratio of background to signal.

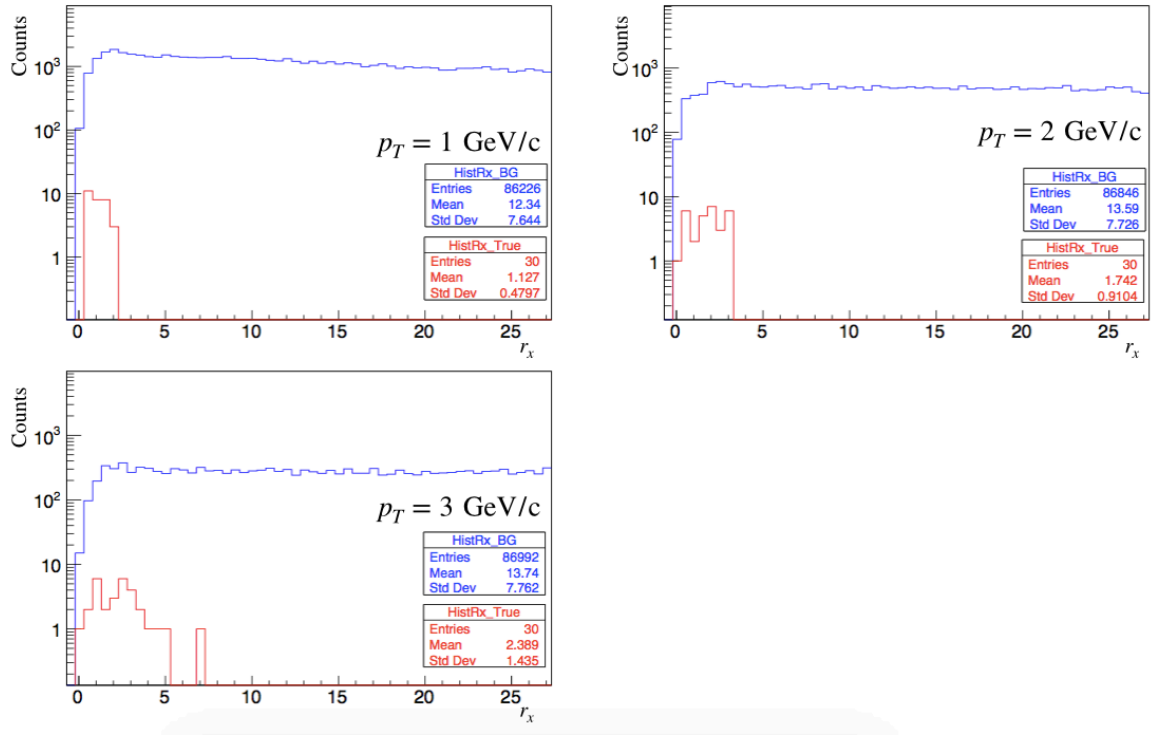

Figure 40: Distribution of r_x. Red line represents embedded muon and blue line represents background. p_T of embedded single muon is shown in each panel.

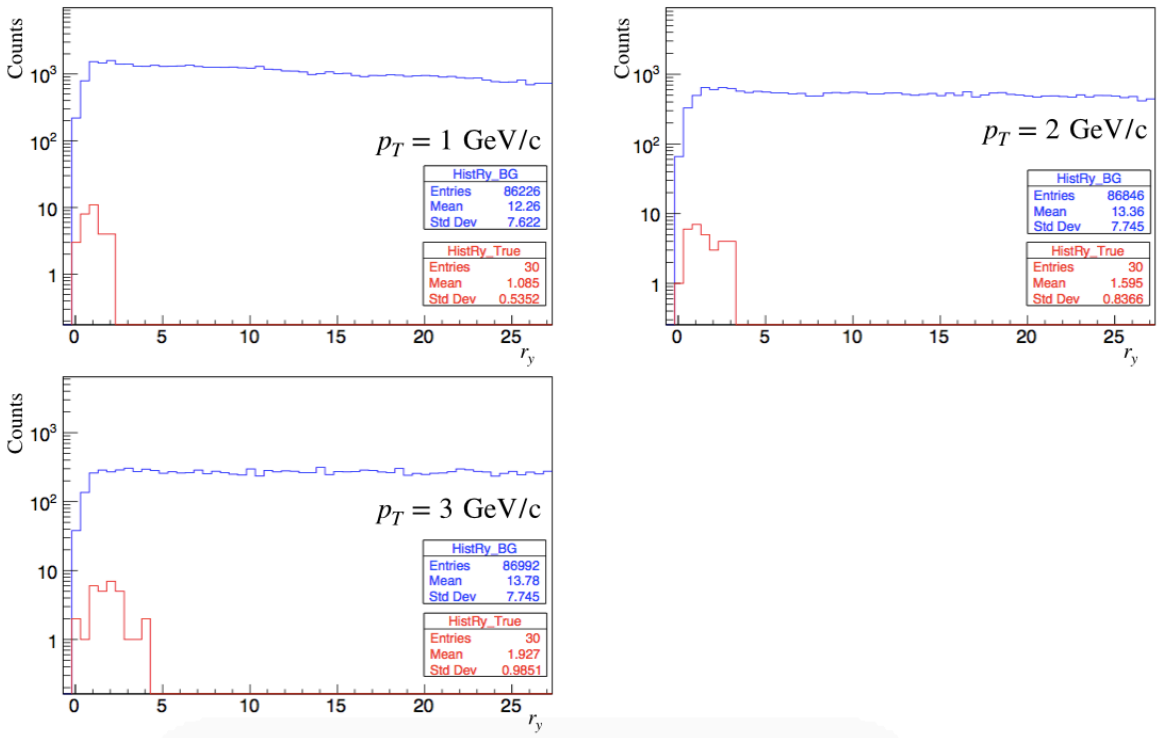

Figure 41: Distribution of r_y. Red line represents embedded muon and blue line represents background. p_T of embedded single muon is shown in each panel.

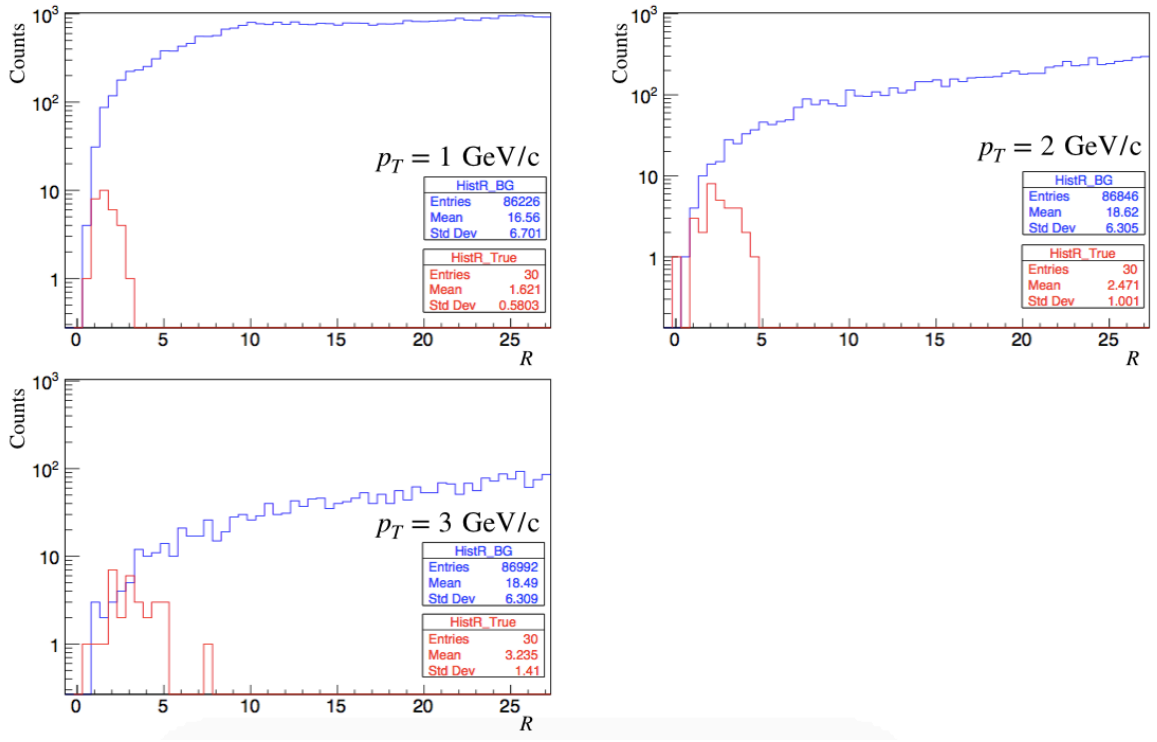

Figure 42: Distribution of R. Red line represents embedded muon and blue line represents background. p_T of embedded single muon is shown in each panel.

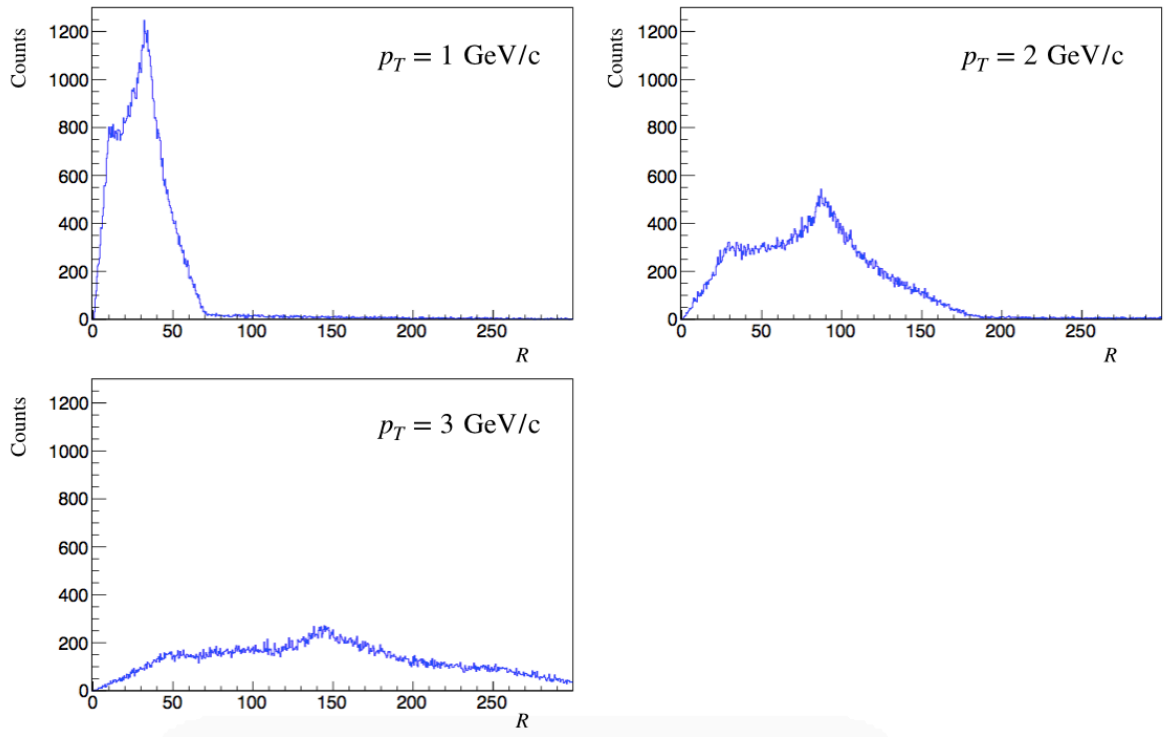

Figure 43: Distribution of R only for background. p_T of embedded single muon is shown in each panel.

Figure 44 shows the ranking of how small R of the embedded muon is among all entries. The possibility that the true MFT track is chosen as the best MFT track significantly increases as p_T increases because the size of the search window is smaller for larger p_T. matching between MFT and MUON. Background can be halved by the sign of charged particle.

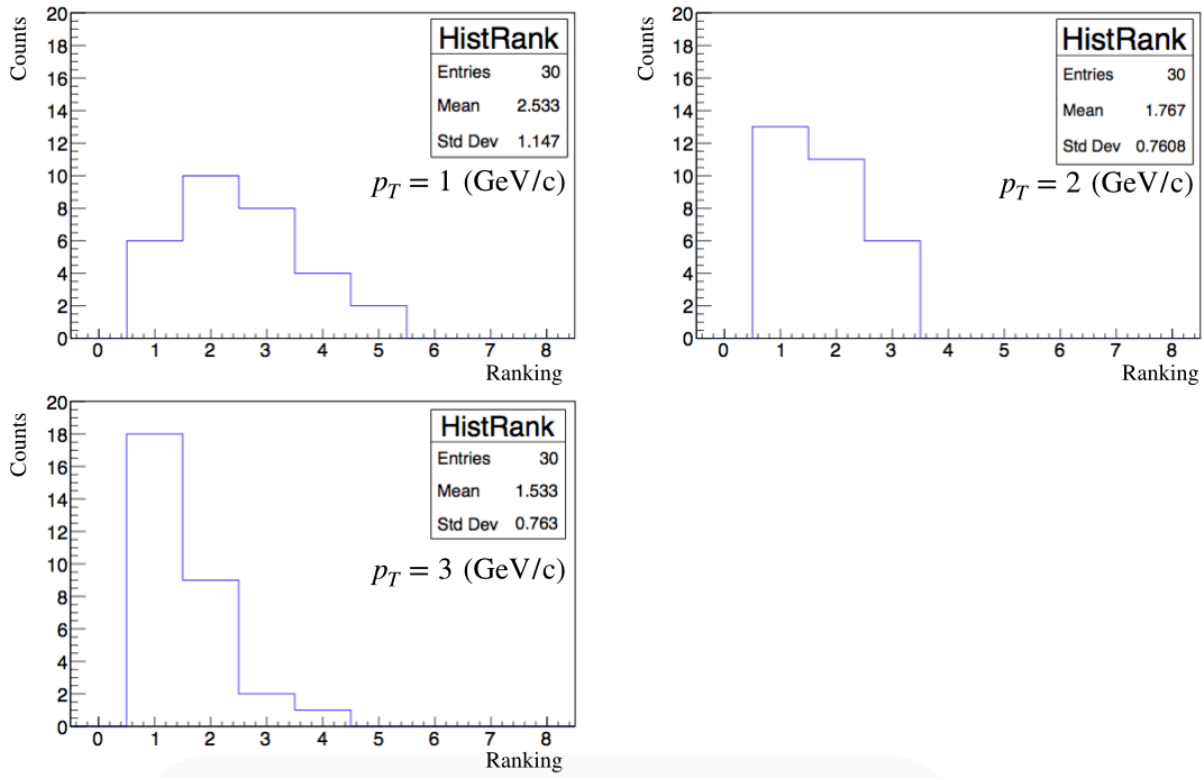

Figure 44: Ranking of how small the two-dimensional matching quality parameter R of the embedded muon was among all entries. p_T is shown in each panel.

5 Summary and Outlook

In this study, the track matching algorithm between MFT and MUON using the correlation between track position and angle is developed. Track matching between MFT and MUON is important for precise tracking around the vertex and to improve signal-to-noise ratio S/N and mass resolution. The number of both MFT track candidates was calculated when using the correlation and when not using. The matching method using the correlation between track position and angle can improve S/N significantly about 6 times with high efficiency.
The developed track matching method must be implemented in the matching algorithm. The MFT track that is the nearest to the center of the distribution is the best. To calculate the distance from the center of the ellipse is harder than calculating the distance from the center of the circle. To make analysis easier, elliptical distribution is converted to circular distribution. After conversion from elliptical to circular distribution, contour lines of efficiency can be written regardless of transverse momentum. Therefore the distance between the center and the track point in the circular distribution is the likelihood of the MFT track candidate regardless of p_T.
The developed matching method is evaluated using HIJING. The matching quality parameter R is developed. The possibility that the true MFT track is chosen as the best MFT track significantly increases with p_T increasing. In evaluation, the ranking of how small matching quality parameter R of the embedded muon is among all entries is calculated.
Here's what we can do as a next step. When matching quality parameter R of the true MFT track is second, that matching quality parameter R may be close to the value of the first matching quality parameter R. A comparison of the difference between R for the true MFT track and background can give other matching quality parameters. In this simulation, true positions and momentum vectors from simulated information not reconstructed information are used at the last MFT disk and the first MUON tracking chamber. Reconstructed standalone tracklets of MFT and MUON are considered the position resolution of detectors. Therefore R should be worse than this evaluation when using reconstructed information. We have to check how well R works when using reconstructed standalone tracklets. Also, a magnetic field is applied parallel to the beam axis. Charged particles are deflected by a magnetic field, especially for low momentum. MFT and MUON can measure the sign of charged particle, therefore the background can be halved. Rough momentum matching between MFT and MUON can reduce background. Also, we need more statistics to evaluate the developed matching method more precisely. The MFT is installed in 2020 and LHC-Run 3 will start in 2021. Therefore the new matching method must be implemented in the matching algorithm before LHC-Run 3.

Acknowledgement

I wish to express my sincere appreciation to Prof. Kenta Shigaki. He invited me to this research and always supervised me despite being in a different university. I would like to thank Asst. Prof. Maya Shimomura and Asst. Prof Takashi Hachiya for always supporting me nearby. Without their support, I could not finish this work. I would like to thank Dr. Yorito Yamaguchi for his various advice from physics to presentation materials.
Prof. Hisaki Hayashii and Prof. Kenkichi Miyabayashi gave different perspective comments. That helped me to understand my work better. I would like to thank Kosei Yamakawa san and Takumi Osako kun who instructed me analysis framework of ALICE. I also would like to thank my colleagues in Nara and Hiroshima. Thanks to them, I could enjoy this two years more. Finally, I must express my gratitude to my family, Tsutomu, Rumi, and Saki. They have always supported what I want to do.
この研究を支えてくださった全ての方々に感謝しています。ありがとうございました。

References

[1] ALICE Collaboration, "Technical Design Report for the Muon Forward Tracker" , CERN-LHCC-2015-001

[2] ALICE Collaboration, "Addendum of the Letter of Intent for the upgrade of the ALICE experiment : The Muon Forward Tracker" , CERN-LHCC-2013-014

[3] M. Kuroda, "ALICE 実験前方ピクセル検出器導入時の物理性能評価", Master thesis, Hiroshima University, (2018).

[4] "Phase diagram of QCD matter : Quark-Gluon Plasma" https://cds.cern.ch/record/2025215.

[5] Tapan K. Nayak, "HeavyIons: Results from the Large Hadron Collider", arXiv:1201.4264 (2012).

[6] C. Quigg, "Spontaneous Symmetry Breaking as a Basis of Particle Mass", arXiv:0704.2232 (2007).

[7] "物質に質量を与えるクォーク凝縮現象を支持する実験的証拠を得ることに成功", https://www.s.u-tokyo.ac.jp/ja/press/2004/02.html.

[8] "Hadron Properties in Nuclear Matter and Dilepton Emission in Relativistic Heavy-Ion Collisions", http://niham.nipne.ro/rp9/

[9] X. Zhu, "D$\bar{\text{D}}$ correlations as a sensitive probe for thermalization in high energy nuclear collisions", Phys.Lett.B. 647 (2007) 366-370.

[10] KEK-PS E325 Collaboration, ”Evidence for In-Medium Modification of the ϕ Meson at Normal Nuclear Density”, Phy. Rev. Lett. 98, 042501, 2007.

[11] "The CERN accelerator complex", https://cds.cern.ch/record/2197559.

[12] "Longer term LHC schedule", https://lhc-commissioning.web.cern.ch/lhc-commissioning/schedule/LHC-long-term.htm.

[13] A. Uras, "The ALICE MFT Project: Motivations and Expectations", http://llr.in2p3.fr/sites/qgp2012/Talks/Etretat_2012_Uras2.pdf.

[14] ALICE Collaboration, "Centrality dependence of the pseudorapidity density distribution for charged particles in Pb-Pb collisions at $\sqrt{s_{NN}}$ = 5.02 TeV", Phys.Lett. B772 (2017) 567-577.

[15] H. Bichsel, D.E. Groom, and S.R. Klein, "27. Passage of particles through matter", http://pdg.lbl.gov/2005/reviews/passagerpp.pdf.

[16] S. Agostinelli *et al.* (GEANT4 Collaboration), "GEANT4: A Simulation toolkit," Nucl. Instrum. Meth. A **506**, 250 (2003).

[17] J. Allison *et al.*, "Geant4 developments and applications," IEEE Trans. Nucl. Sci. **53**, 270 (2006).

[18] X. Wang and M. Gyulassy, "HIJING 1.0: A Monte Carlo Program for Parton and Particle Production in High Energy Hadronic and Nuclear Collisions", arXiv:nucl-th/9502021 (1995).